eLife

Reviewed Preprint
v1 • August 19, 2026
Not revised

For correspondence:
kellym@ohsu.edu

Present address: Department of Biology, Appalachian State University, Boone, North Carolina, USA

* Present address: Department of Chemistry & Biochemistry, Bates College, Lewiston, Maine, USA

† These authors contributed equally to this work

Competing interests: No competing interests declared

Funding: See page 20

Reviewing editor: Sameh Ali, Children's Cancer Hospital Egypt, Egypt

Identifying Novel Estrogenic Mitochondrial Targets in Hypothalamic Proopiomelanocortin Neurons by Chemoproteomics

Jian Qiu[1,†], Martha A Bosch[1,†], Mya Wolfe[2,†], Ksenija Korac[3,†], Stefano Rizzo[4], Todd L Stincic[1,#], Scotland E Farley[1,*], Wendy Fitzgerald[2], Megha Rajendran[2], Aurélien Laguerre[1], Frank Stein[5], Philip F Copenhaver[6], Oline K Rønnekleiv[1], Sean M Rønnekleiv-Kelly[3], Tatiana K Rostovtseva[2], Sergey M Bezrukov[2], Carsten Schultz[1], Martin J Kelly[1]

[1]Department of Chemical Physiology and Biochemistry, Oregon Health & Science University, Portland, United States • [2]Euince Kennedy Shriver National Institute of Child Health & Human Development, NIH, Bethesda, United States • [3]Department of Surgery, U. Wisconsin School of Medicine, Madison, United States • [4]Sirius Fine Chemicals SiChem GmbH, Bremen, Germany • [5]European Molecular Biology Laboratory, Cell Biology & Biophysics Unit, Heidelberg, Germany • [6]Department of Cell, Developmental & Cancer Biology, Oregon Health & Science University, Portland, United States

eLife Assessment

This **useful** study employs an innovative chemoproteomic and multi-modal experimental approach to support VDAC2 as a key functional mediator of STX effects on mitochondrial bioenergetics. However, concerns remain regarding the physiological and disease relevance, including the reliance on cell lines, lack of loss-of-function validation, unresolved binding specificity, and limited justification for focusing on POMC neurons in the context of Alzheimer's disease. As a result, the evidence is **incomplete** for a link between VDAC2 and Alzheimer's pathogenesis, and aspects of the binding data raise alternative interpretations, including a potential role for other VDAC isoforms.

https://doi.org/10.7554/eLife.111731.1.sa2

Abstract

Loss of estrogens at menopause is linked to impaired brain metabolism and increased risk of Alzheimer's disease (AD). However, estrogen replacement therapies are limited due to the deleterious effects of estrogen on peripheral organs and increased risk of vascular dementia. We have developed a non-steroidal estrogenic compound, STX, which does not bind to the classical estrogen receptors α and β, but mimics estrogenic signaling in the central nervous system (CNS) without the peripheral reproductive actions. STX is protective against neurodegeneration in stroke and AD models, but its molecular targets are unknown. Here, we identified and validated STX neural targets using chemoproteomic, molecular biological, electrophysiological and metabolic assays of hypothalamic proopiomelanocortin (POMC) neurons. Chemoproteomic profiling identified voltage dependent anion channels (VDAC1-3) as major intracellular binding partners in mHypo43 (POMC) cells. Based on quantitative single-cell PCR, *Vdac2* was identified as the dominant isoform in female hypothalamic POMC neurons. Seahorse metabolic flux analyses showed that STX potently increased glycolysis, oxidative respiration and mitochondrial ATP production in mHypo43 cells. Nanomolar concentrations of STX enhanced VDAC2 voltage-dependent gating in reconstituted lipid membranes and shifted the low-conductance states toward anion selectivity, consistent with increased ATP flux. Together, these findings reveal a mechanism for the neuroprotective effects of STX through enhancing mitochondrial bioenergetics and

modulating VDAC channel properties, potentially increasing cellular energy stores. Therefore, this work identifies previously unrecognized estrogenic mitochondrial targets and provides a mechanistic basis for the neuroprotective actions of STX relevant to menopause-associated brain vulnerability.

Introduction

Approximately two-thirds of patients with Alzheimer's disease (AD) are women, and the loss of the ovarian steroid 17β-estradiol (E2) at menopause is strongly associated with increased vulnerability to neurodegeneration (Nebel et al., 2018). Although E2 replacement is neuroprotective in animal models, including non-human primates (Rapp et al., 2003; Morrison et al., 2006), hormone replacement therapy in post-menopausal women has produced adverse outcomes, including increased risk of coronary heart disease and vascular dementia (Rossouw et al., 2002; Shumaker et al., 2003). These limitations have driven the development of neuroprotective selective estrogen receptor modulators (SERMs), but most act through nuclear estrogen receptors and retain undesirable peripheral effects (Murphy et al., 2003).

In search of a selective neuroprotective SERM, we developed STX, a synthetic diphenyl acrylamide compound that selectively targets the central nervous system (CNS) and mimics the rapid, membrane-initiated estrogen signaling without activating classical estrogen receptors (Qiu et al., 2003; Qiu et al., 2006; Tobias et al., 2006; Roepke et al., 2010; Smith et al., 2014). STX activates G protein–coupled signaling pathways in hypothalamic neurons (Qiu et al., 2003; Qiu et al., 2006; Smith et al., 2013). In proopiomelanocortin (POMC) neurons, STX induces heterologous desensitization of inhibitory $G\alpha_{i/o}$-coupled receptors, including μ-opioid and $GABA_B$ receptors, thereby increasing neuronal excitability (Qiu et al., 2003; Qiu et al., 2006). Importantly, STX crosses the blood–brain barrier, can be administered chronically, and reproduces key estrogenic effects on thermoregulation and metabolism without peripheral estrogenic actions (Roepke et al., 2010).

In addition to its rapid neuromodulatory effects, STX exhibits robust neuroprotective properties. It reduces ischemic neuronal damage in hippocampal neurons (Lebesgue et al., 2010), enhances synaptic plasticity, and protects against β-amyloid toxicity in cellular and animal models of AD (Gray et al., 2016; Quinn et al., 2022; Lee et al., 2025). These effects are accompanied by improvements in mitochondrial function, suggesting that regulation of cellular bioenergetics may be a central component of STX action. Mitochondrial dysfunction is a defining feature of neurodegenerative diseases (Ashleigh et al., 2023), and declines in brain metabolic capacity are strongly associated with menopause (Brinton et al., 2015; Mosconi et al., 2018). However, the molecular targets through which STX modulates mitochondrial function and neuronal activity remain unknown.

A key regulator of mitochondrial metabolism is the voltage-dependent anion channel (VDAC), located in the outer mitochondrial membrane. VDACs control the exchange of ATP, ADP, and other metabolites between mitochondria and the cytosol, thereby governing cellular energy homeostasis (Rostovtseva and Colombini, 1996; Colombini, 2004; Rostovtseva and Bezrukov, 2008). Modulation of VDAC gating and ion selectivity can directly influence mitochondrial respiration and metabolic flux. Although steroidal compounds have been reported to bind VDACs, their functional effects on channel activity are limited (Camara et al., 2017; Reina and De Pinto, 2017; Rostovtseva et al., 2020). In isolated liver mitochondria, the non-steroidal SERM tamoxifen has been shown to bind to VDACs and potentially regulate transport of anions across the mitochondrial membrane (Unten et al., 2022).

However, identifying the molecular targets of small molecules such as STX in intact cells remains a major challenge. Unlike protein–protein interactions, small molecule–protein interactions are often transient and difficult to capture biochemically. Diazirine-based photoaffinity labeling, combined with biorthogonal click chemistry, enables covalent capture and enrichment of ligand-bound proteins in living systems (Moellering and Cravatt, 2012; Schultz et al., 2022). This

"flash-and-click" strategy has proven effective for mapping lipid and small-molecule interactomes in complex cellular environments (Haberkant et al., 2013; Hulce et al., 2013; Höglinger et al., 2017; Müller et al., 2020; Müller et al., 2021).

Therefore, we combined chemoproteomics, molecular biology, electrophysiology and mitochondrial physiology to identify the cellular targets of STX in hypothalamic POMC neurons. Using a photoactivatable STX probe, we identified all three VDAC isoforms as prominent intracellular binding partners. We show that STX directly modulates mitochondrial VDAC channels, enhancing voltage-dependent gating and altering ion selectivity, with corresponding increases in mitochondrial ATP production, respiratory capacity and glycolytic function.

Results

Chemoproteomic identification of STX targets reveals VDACs as prominent binding partners

In order to see if STX binds to VDACs similar to the structurally-related tamoxifen (Unten et al., 2022), we designed a novel bifunctional STX derivative (BF-STX) containing both a photo-cross-linkable diazirine group and an alkyne handle, which was synthesized in collaboration with SiChem GmbH (Germany) (Figure 1A). BF-STX retained full biological activity, reproducing the ability of STX to induce heterologous desensitization of Gi/o-coupled receptor signaling in POMC neurons, which inhibits the activity of these anorexigenic neurons (Qiu et al., 2003; Qiu et al., 2006) (Figure 1B). Also, with UV activation BF-STX enabled robust and cell-type–specific labeling in hypothalamic slices from female BL6 mice and mHypo43 cells (Figures 1C,D).

To identify candidate STX-binding proteins, mHypo43 POMC cells were incubated with BF-STX (10 μM) for 30 min and then exposed to UV light (350 nm) to induce crosslinking (Figure 2A). Negative controls included samples without UV exposure and cells incubated with BF-STX together with a 3-fold higher concentration of STX. These controls ensured that the enriched hits were legitimate targets and not "off-targets" from photo-crosslinking (Kleiner et al., 2017; West et al., 2021). Protein–BF-STX conjugates were labeled via click chemistry using picolyl-azide agarose beads, digested on-bead, TMT-labeled, and analyzed by LC-MS/MS on an Orbitrap Fusion Lumos system at EMBL as described in the Materials and Methods. VDAC1, VDAC2, and VDAC3 emerged as prominent targets (Figure 2A, Suppl Table 1). Interestingly, even with a short exposure (5 min) to BF-STX, VDACs emerged as a significant targets (Figure 2B, Suppl Table 2), which is congruent with the rapid neuroprotective actions of STX to rescue CA1 hippocampal neurons following global ischemia in female rats (Lebesgue et al., 2010). Furthermore, fold-change correlation plots showed that VDAC proteins were strongly enriched in the UV crosslinking condition relative to the no-UV control (x-axis), while enrichment was reduced in the competition experiments, shifting the VDAC proteins toward the x-axis. This pattern is consistent with competition-sensitive BF-STX labeling (Figure S4A). Moreover, a heatmap plot of the binding (Figure S4B) revealed that when unlabeled STX (1 or 3 molar equivalents) was added, the signal for VDACs faded. This competition pattern is consistent with partial reduction of BF-STX enrichment in the presence of unlabeled STX.

VDAC2 is the predominant isoform expressed in POMC neurons

At the molecular level, we first examined whether VDACs are expressed in hypothalamic anorexigenic POMC neurons, given their central role in mitochondrial metabolite exchange. Single-cell qPCR from pooled POMC neurons from female mice revealed a clear expression hierarchy, with *Vdac2* ≥ *Vdac3* >> *Vdac1* mRNA (Figures 3A,B), indicating that VDAC2 is the dominant isoform in this neuronal population. This distribution contrasts with most tissues, where VDAC1 predominates (Zinghirino et al., 2021), suggesting a cell-type–specific specialization of mitochondrial outer membrane channels in POMC neurons.

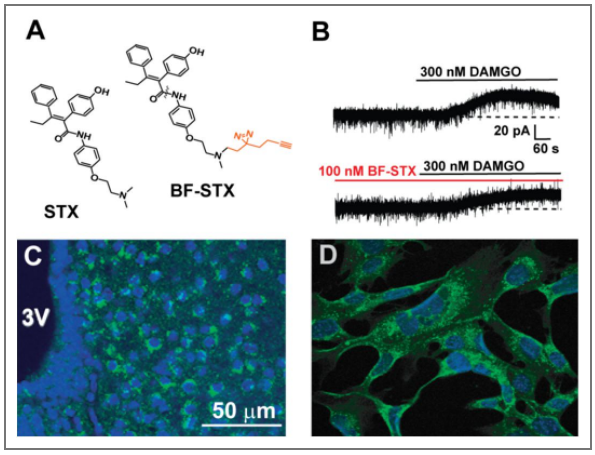

Figure 1. Design, stability, and functional characterization of photoreactive bifunctional-STX (BF-STX) in neurons and cell lines.

A. Chemical structures of STX and bifunctional-STX (BF-STX), featuring a diazirine group connected to an alkyne handle (both shown in red) for photo-crosslinking and click chemistry, respectively. Upon 7 minutes under 350 nm UV illumination in methanol (MeOH), BF-STX exhibited characteristic changes in proton resonances near the diazirine moiety, confirming photoreactivity (see Supplemental Files). BF-STX remained chemically stable in the dark. **B.** BF-STX rapidly attenuated μ-opioid receptor–mediated responses in $POMC^{EGFP}$ neurons. The μ-opioid receptor, like the $GABA_B$ receptor, is $G_{i/o}$-coupled and activates G protein-coupled, inwardly rectifying K^+ (GIRK) channels in $POMC^{EGFP}$ neurons. In voltage-clamp recordings (V_{hold}= -60 mV), an EC_{50} concentration of DAMGO (a μ-opioid receptor agonist) elicited GIRK-mediated outward currents (top trace), which were reduced by 38.7 ± 5.7 % (n=3) following a 15-minute exposure to BF-STX. This heterologous desensitization is consistent with previous observations using the BF-STX parent compound, STX, which causes a 41% attenuation in the $GABA_B$ (and μ-opioid) receptor-mediated activation of GIRK channels in POMC neurons (Qiu et al., 2003). **C,D.** Confocal images showing subcellular accumulation of BF-STX (10 μM, 30 min). BF-STX treated cells were subjected to UV crosslinking (2.5 min at 350 nm, on ice), cell fixation, and fluorescent labelling via copper-click reaction using picolyl-azide Alexa Fluor 488. **C.** In hypothalamic slices, BF-STX selectively labeled POMC neurons near the third ventricle (3V). **D.** BF-STX labeled mHypo43 cells.

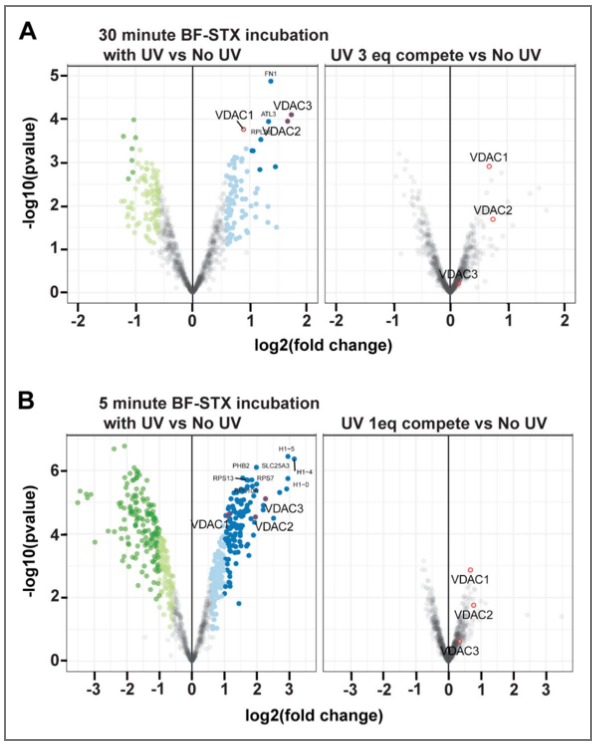

Figure 2. Chemoproteomic identification of BF-STX–interacting proteins in mHypo43 cells following UV crosslinking.

A. Volcano plots showing enriched proteins identified after 30 min BF-STX incubation under UV crosslinking conditions compared with no-UV controls (left), and after competition with 3× excess unlabeled STX during UV crosslinking compared with no-UV controls (right). Proteins significantly enriched by BF-STX labeling are highlighted, with VDAC1, VDAC2, and VDAC3 among the prominent candidate targets identified after UV exposure. Competition with excess STX reduced enrichment of VDAC family proteins, consistent with competition-sensitive BF-STX labeling. **B.** Volcano plots showing enriched proteins identified after 5 min BF-STX incubation under UV crosslinking conditions compared with no-UV controls (left), and competition with 1× excess unlabeled STX during UV crosslinking compared with no-UV controls (right). Shorter BF-STX incubation increased enrichment and statistical significance of VDAC1, VDAC2, and VDAC3. Competitive STX treatment reduced enrichment of these proteins, consistent with BF-STX associated labeling of VDAC family members. The x-axis represents log2 (fold change), and the y-axis represents –log10 (p value).

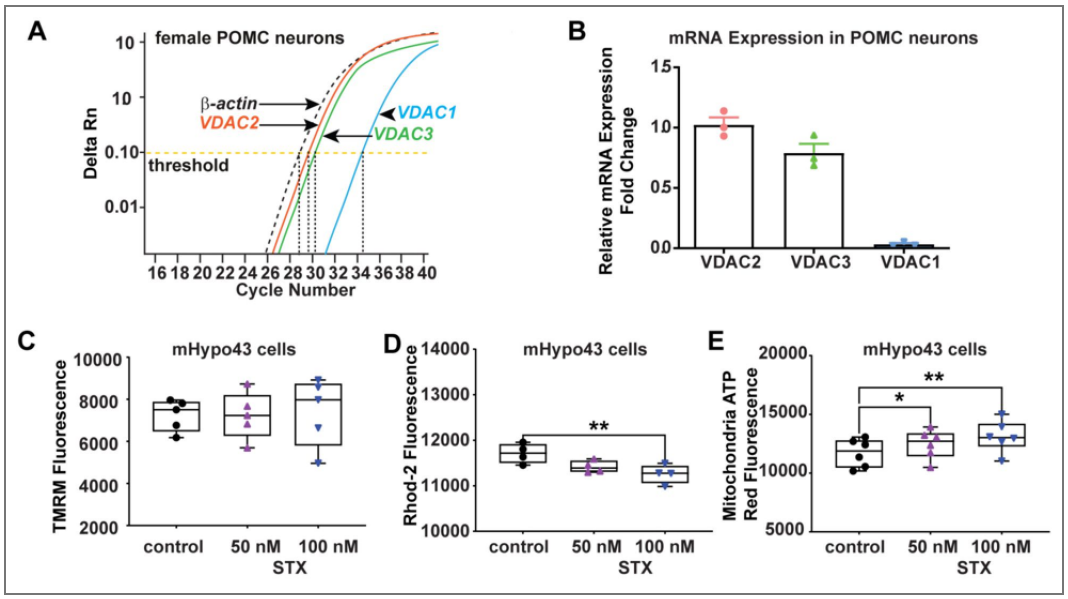

Figure 3. qPCR identification of VDAC1-3 as targets in POMC neurons

A. Quantitative PCR (qPCR) amplification curves for VDAC1-3 were generated from 10-cell pools of *Pomc*^{EGFP} neurons in female mice. Cycle number was plotted against normalized fluorescence intensity (ΔRn) to visualize amplification, with the cycle threshold (Ct; dashed line) indicating the point at which fluorescence exceeded background levels and sample values were quantified. **B**. Summary bar graphs of relative expression of *Vdac2, Vdac3, Vdac1* mRNA in female POMC neurons. **C**. Mitochondrial membrane potential determination using TMRM dye; **D.** Mitochondrial calcium using Rhod2 dye; and **E,** mitochondrial ATP using BioTracker ATP-Red live cell dye were measured in mHypo43 cells upon treatment with 50 and 100 nM STX. Data from 4-6 independent experiments are represented in the box plots. The symbols represent data from each repeat, the borders of the boxes define the 25th and 75th percentiles, with the median displayed as black lines, and error bars indicate the standard deviation from the mean. Statistical analysis was peformed using one-way ANOVA followed by the Dunnett *post hoc* test (**p<0.01, *p<0.05).

To assess whether STX influences mitochondrial function in these cells, we measured mitochondrial membrane potential, calcium and ATP levels in mHypo43 neurons. STX (100 nM) did not alter the mitochondrial membrane potential, but it significantly reduced mitochondrial calcium concentrations and increased mitochondrial ATP levels (Figures 3C-E). These findings indicate that STX enhances mitochondrial function without inducing depolarization, consistent with improved metabolic efficiency rather than mitochondrial stress.

STX directly modulates VDAC2 channel gating and ion selectivity

To determine whether STX directly targets VDAC channels, we performed electrophysiological recordings of recombinant human VDAC2 reconstituted in planar lipid membranes (Figure 4A) (Rostovtseva and Bezrukov, 2015). We focused on VDAC2, which had the highest mRNA expression in POMC neurons (Figure 3A,B). In a symmetrical 1 M KCl buffer solution, VDAC2 typically forms channels of ~3.5 – 4.0 nS conductance (Figure 4A) (Rosencrans et al., 2025), which characteristically transition (*i.e.*, gate) from the high conducting "open" state to a variety of lower-conducting or "closed" states in response to large applied voltages (Figure 4B, control trace). Under these experimental conditions, the application of 60 mV was required to observe consistent voltage gating. For the sake of illustrative clarity, in Figure 4B we show traces at negative potentials. The addition of 100 and 300 nM STX to the "cis" (grounded) side (Figure 4A) of the membrane caused channel closure at lower negative potentials, -20 and -10 mV, respectively (Figure 4B, lower traces). The transitions to the low conductance states were reversible such that the voltage jump to 0 mV fully reopened the channel, a characteristic behavior of reconstituted VDACs (Colombini, 1989). The single-channel recordings revealed that in the presence of STX, voltages of 40-50 mV lower than those in the control were sufficient for VDAC2 single-channel gating.

A quantitative analysis of the reconstituted VDAC voltage gating requires recording from many channels, which is best achieved using a multichannel approach (Rostovtseva et al., 2006; Teijido et al., 2014; Rappaport et al., 2015). In this protocol, slow triangular voltage waves (5 mHz, ±60 mV) are applied to the membrane containing 20-100 channels. Figure 4C shows representative normalized conductance-voltage plots of G/G_{max} versus voltage at negative potentials, where G is the conductance at a given voltage, and G_{max} is the maximum conductance at voltages close to 0 mV, in control and after addition of 50, 100, and 1000 nM STX to the cis compartment. The STX-enhanced voltage gating was manifested as a decrease in the minimal conductance (G_{min}, indicated by dashed gray lines) calculated at $|V| >$ between 45-55 mV (downward arrow in Figure 4C). The dose-dependence of STX-enhanced VDAC2 voltage gating was quantified as the normalized change in conductance $(G_{max}\text{-}G_{min})/G_{min}$ plotted against STX concentrations (Figure 4D). The averaged normalized reduction in G_{min} with STX concentration was approximated by a first-order binding curve with a K_d of 15 ± 4 nM.

These results suggested a direct functional interaction between STX and VDAC2. To further test this hypothesis, we measured the ionic selectivity of VDAC2 in the presence of STX. The open state of VDAC2, similarly to VDAC1 and VDAC3 (Tan and Colombini, 2007; Queralt-Martín et al., 2020; Rosencrans et al., 2025), is anion-selective, and multiple voltage-induced closed states are characterized by a wide range of low conductances and predominantly cationic selectivity (Colombini, 1989). We measured VDAC2 selectivity in a 5x salt gradient, 1 M KCl (cis side) versus 0.2 M KCl (trans side). A representative trace of VDAC2 obtained in this salt gradient before and after the addition of 100 nM STX to the cis compartment is shown in Figure 4E. In the presence of STX, the fluctuations of channel conductance between different conductance levels were measured at ±10 mV. The corresponding I/V plots for the open and the three low-conducting states are shown in Figure 4F. The linear regressions through the data points determined the substate conductance as a slope, and the reversal potential Ψ_{rev} as the voltage at which the current is zero for each substate. While the selectivity of the open state (1.9 nS) remained unchanged (Ψ_{rev} = 8.3 mV), in the presence of STX two low-conducting states of 0.5 and 0.6 nS displayed anion selectivity

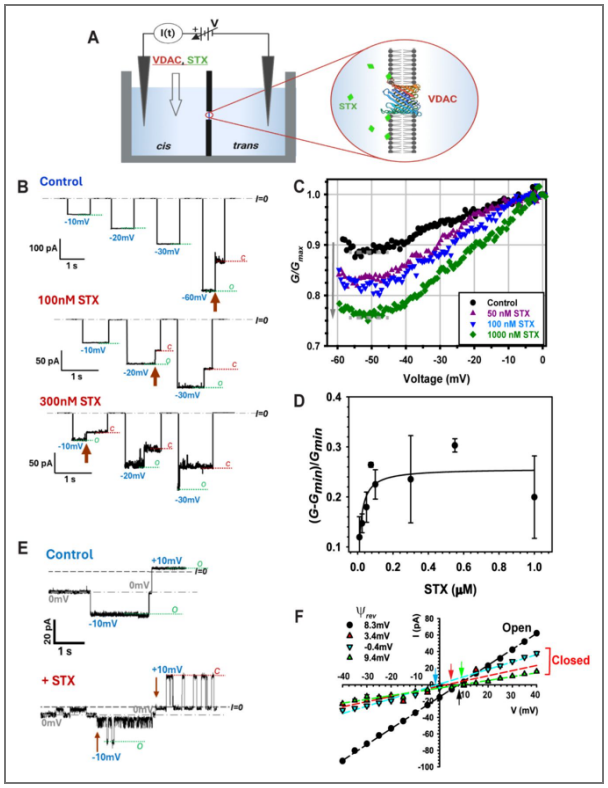

Figure 4. STX promotes voltage gating of VDAC2 and shifts the channel's low conducting states towards anion selectivity.

A. A schematic of the experimental setup for VDAC reconstitution. In these experiments, a single VDAC spans a planar lipid membrane that separates and electrically isolates two buffer-filled compartments. The ionic current through the channel is generated by the applied voltage and constantly recorded. VDAC and STX (green diamonds) were added to the cis compartment. **B.** Electrophysiological recordings of the recombinant human VDAC2 reconstituted into planar lipid membranes before (Control) and after the addition of 100 and 300 nM STX to the membrane-bathing solution. The current traces, representing two VDAC2 channels, were recorded on the same membrane at the indicated voltages, which were returned to 0 mV between each subsequent voltage application. Characteristic voltage-gating behavior is seen as a stepwise current transition from the unique high-conducting or "open" state ("o" state, indicated by green dashed lines) to a low-conducting "closed" state ("c" state, indicated by red dashed lines). The lowest voltages at which gating was observed at each condition are indicated by red arrows. Here and in panel E, the dash-dotted gray lines show the zero current level (I=0). Membrane bathing solutions contained 1 M KCl buffered with 5 mM HEPES at pH 7.4. **C.** The normalized VDAC2 conductance as a function of the applied voltage obtained in a representative experiment with about 60 VDAC2 channels reconstituted into a planar membrane without (Control) and with subsequent additions of 50, 100, and 1000 nM of STX. Normalized conductance is defined as G/G_{max}, where G is the average conductance at voltage V, and G_{max} is the maximum average conductance at voltages close to 0 mV. Gating behavior was assessed by applying a triangular voltage wave of ±60 mV, 5 mHz. The addition of STX resulted in a decrease in the minimal (G_{min}) normalized conductance (indicated by dashed gray lines) at the application of negative voltages (emphasized by the downward arrow), indicative of increased gating. These results, obtained in multichannel membranes, are consistent with the single-channel records in B. Other experimental conditions were as in (B). **D**. STX promotes VDAC2 voltage gating in a dose-dependent manner. Normalized gating response of four independent experiments, as in (C), represented as $(G_{max}\text{-}G_{min})/G_{min}$ and plotted against increasing concentrations of STX. Each data point denotes the mean ± SD (n=4). The line is a ligand-binding, one-site saturation curve with K_d = 15 ± 4 nM. **E,F** STX affects the ion selectivity of VDAC2 voltage-induced "closed" states. **E.** Representative single-channel trace obtained in 1 M (cis)/ 200 mM (trans) KCl gradient before (Control, upper trace) and after (+ STX, lower trace) addition of 100 nM STX to the cis compartment at the indicated voltages. Dashed green and red lines indicate open and "closed" states, respectively; dashed gray lines indicate zero current. A planar lipid membrane was formed from DPhPC. **F.** I/V curves obtained from the traces, examples of which are shown in E, for the open (black circles) and three closed (triangles) states. Linear regressions (dashed lines) allow calculation of the reversal potential (ψ_{rev}, indicated by arrows) of each state (shown in the inset). A positive ψ_{rev} corresponds to anionic and a negative to cationic selectivity. The open state with conductance of 1.9 nS is anion selective (ψ_{rev} = 8.3 mV); two low-conducting states of 0.5 and 0.6 nS are also anion selective with ψ_{rev} equal to 9.4 and 3.4 mV, respectively, and the low-conducting state of 0.9 nS conductance, is non-selective (ψ_{rev} = 0.4 mV).

with Ψ_{rev} equal to 9.4 and 3.4 mV, respectively, with one low-conducting state (0.9 nS) being non-selective (inset in Figure 4F). These results indicate that STX may alter the selectivity of VDAC2 closed states, without affecting either the conductance or selectivity of the open state.

The absence of an effect of STX on VDAC2 open-channel conductance suggested that this hydrophobic compound most likely interacts with VDAC2 at the protein-lipid interface. We further postulate that by reversing the selectivity of VDAC2 closed states to anionic, STX modulates the transport properties of VDAC2 to favor ATP flux (Rostovtseva and Colombini, 1996). These results also explain the decreased mitochondrial calcium and increased mitochondrial ATP measured in mHypo43 (POMC) neurons (Figures 3D,E). Facilitation of ATP/ADP fluxes may contribute to the neuroprotective effects of STX in CNS neurons (Gray et al., 2016; Quinn et al., 2022; Lee et al., 2025).

STX enhances mitochondrial respiration and glycolytic function

Based on the findings that STX increased ATP concentrations in mHypo43 cells (Figure 3E), we decided to measure cellular metabolism in real-time using the Agilent Seahorse Assay system. We investigated the effects of STX on mitochondrial function, including mitochondrial respiration and glycolysis over time. Mitochondrial respiration (Figures 5, 6) was assessed by administrating agents that target different components of the electron transport chain (i.e., oligomycin, FCCP and rotenone/antimycin A) (Divakaruni et al., 2014) (see Materials and Methods). These measurements were conducted under control conditions (vehicle) and compared to treatment with 1 nM, 5 nM or 10 nM STX in mHypo43 cells. STX treatment led to an increase in several key parameters of mitochondrial respiration (Figure 5A). Quantitative analysis revealed that STX significantly increased basal respiration (Figure 5B), ATP production (Figure 5C), and maximal respiratory capacity (Figure 5D). Additionally, STX augmented spare respiratory capacity (Figure 5E), suggesting enhanced mitochondrial adaptability under stress conditions. Notably, proton leak (Figure 5G) but not non-mitochondrial respiration (Figure 5F) was significantly increased. Since neurons are highly dependent on glucose uptake and glycolysis as a source of energy (Li et al., 2023), we also analyzed glycolysis by exposing mHypo43 cells to oligomycin, FCCP and rotenone/antimycin A, while measuring the extracellular acidification rate (ECAR) over time. There were differences in ECAR with STX treatment versus control (Figure 5H). The lower concentrations of STX (1 and 5 nM) significantly increased glycolysis (Figure 5I), glycolytic capacity (Figure 5J), glycolytic reserve (Figure 5K) and non-glycolytic acidification (Figure 5L). However, since there was a non-monotonic dose-response to STX, *i.e.* 10 nM STX did not increase glycolytic function, we speculated that the concentration of estrogens in the serum were saturating the STX targets and therefore causing a desensitization. Therefore, we serum-starved the mHypo43 cells for 6 hours prior to the Seahorse Assay in order to remove any endogenous estrogens (Figure 6). The serum starvation did not alter the "bell-shaped" dose-response for glycolytic function (Figures 6H-L) and even showed a monotonic dose-response for mitochondrial respiratory parameters (Figures 6A-G). Since hepatocytes exhibit the highest mitochondrial density within the human body (Xu et al., 2023), we sought to see if STX was equally potent in immortalized human hepatocyte (IHH) cells to increase mitochondrial respiration. Indeed, 1 nM (and 10 nM) STX increased mitochondrial respiration in both serum (Figures S5A-G) and serum-starved conditions (Figures S6A-G). As one would predict, since IHH cells are not dependent on glucose uptake as an energy source, glycolytic function was essentially unaltered with STX treatment in serum (Figures 5H-L) and serum-starved conditions (Figures 6H-L). Collectively, these results indicate that STX acts independently of endogenous estrogenic compounds and are consistent with the fact that neurons require glucose uptake and glycolysis to maintain their electrophysiological activity (Li et al., 2023).

Discussion

A central strength of this study is the use of photoaffinity labeling coupled with click chemistry to capture STX–protein interactions in intact cellular systems. Because small molecule–protein interactions are often weak, reversible and difficult to preserve during biochemical isolation, the

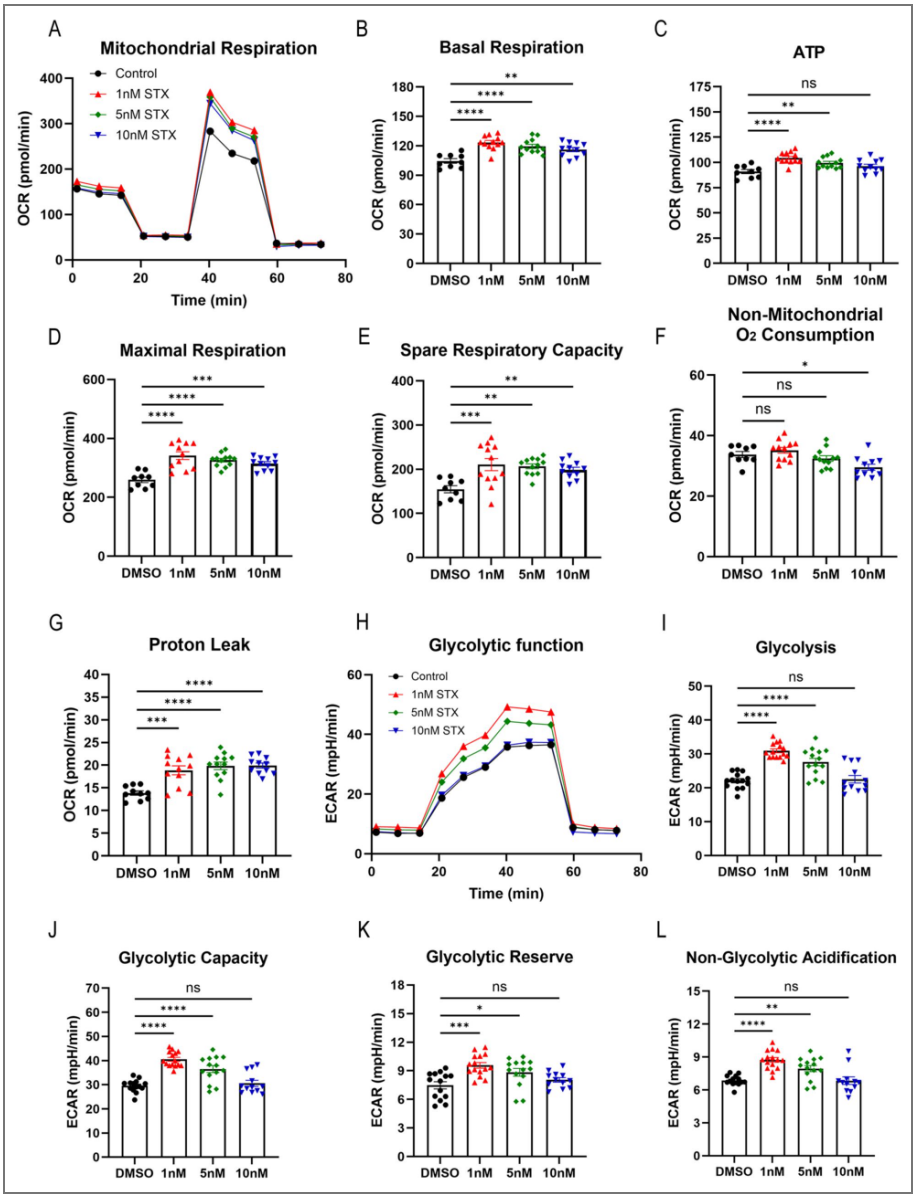

Figure 5. STX induces coordinated mitochondrial and glycolytic activation with a non-monotonic dose–response in non-serum starved mHypo43 cells.

A. Representative Seahorse XF traces of oxygen consumption rate (OCR) in non-serum starved mHypo43 cells treated with DMSO (control) or STX (1, 5, 10 nM). Sequential injections of oligomycin, FCCP, and rotenone/antimycin A were used to assess mitochondrial respiratory function. **B–G**. Quantification of mitochondrial respiration parameters derived from OCR measurements, including basal respiration (**B**), ATP-linked respiration (**C**), maximal respiration (**D**), spare respiratory capacity (**E**), non-mitochondrial oxygen consumption (**F**), and proton leak (**G**). STX treatment significantly increased basal respiration, ATP-linked respiration, maximal respiration, and spare respiratory capacity, with the most pronounced effects observed at 1 nM. These enhancements were maintained, though slightly attenuated, at 5 nM and 10 nM. Proton leak was significantly increased across STX-treated groups, while non-mitochondrial respiration showed modest changes. **H**. Representative extracellular acidification rate (ECAR) traces during the glycolysis stress test under the same treatment conditions. Sequential injections of glucose, oligomycin, and 2-deoxyglucose (2-DG) were used to assess glycolytic function. **I–L**. Quantification of glycolytic parameters derived from ECAR measurements, including glycolysis (**I**), glycolytic capacity (**J**), glycolytic reserve (**K**), and non-glycolytic acidification (**L**). STX at 1 nM and 5 nM significantly increased glycolysis and glycolytic capacity. At 1 nM, STX significantly increased glycolytic reserve and non-glycolytic acidification, with moderate effects observed at 5 nM. No significant enhancement was observed at 10 nM. Data are presented as mean ± SEM with individual data points shown. Statistical significance was determined by one-way ANOVA followed by Dunnett's multiple comparison test. ns-not significant, *p < 0.05, **p < 0.01, ***p < 0.001, ****p < 0.0001.

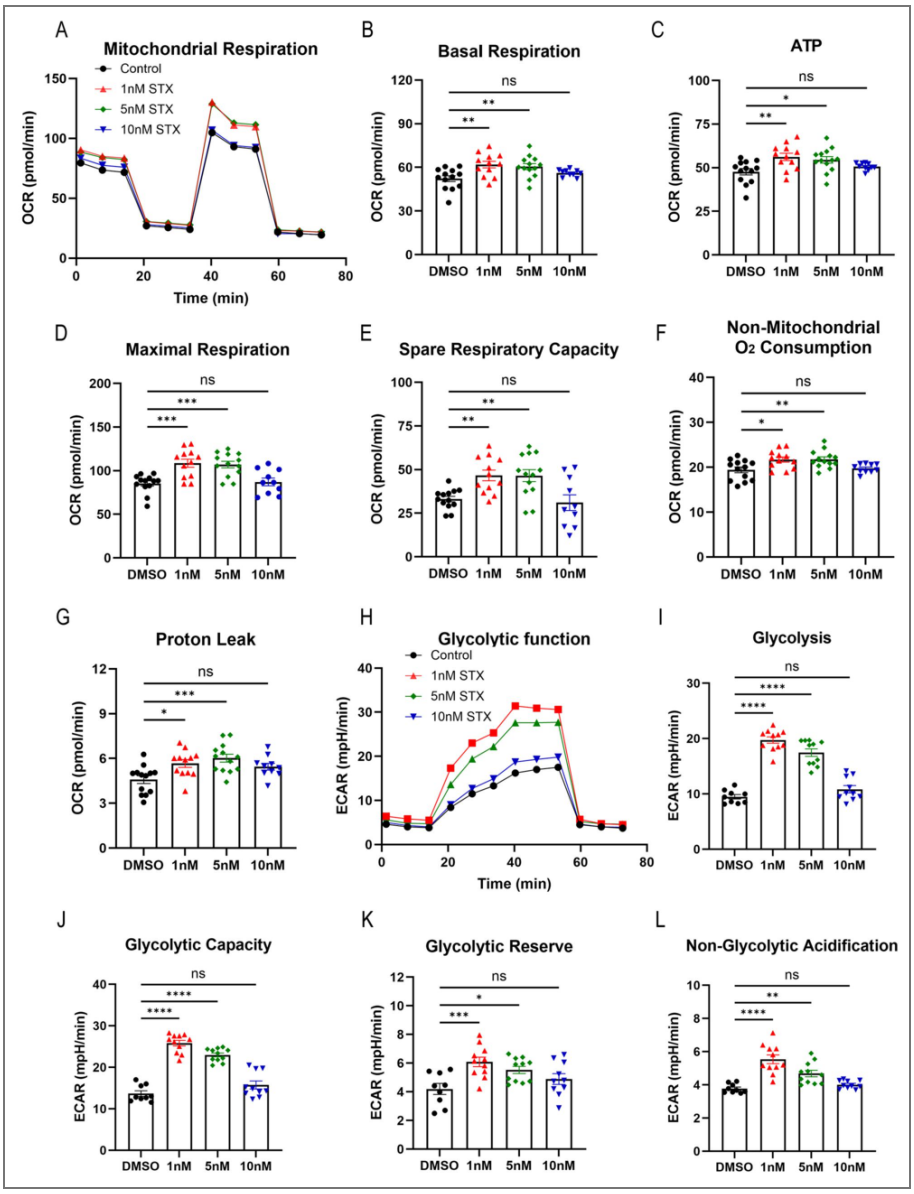

Figure 6. STX induces coordinated mitochondrial and glycolytic activation with a non-monotonic dose–response in serum starved mHypo43 cells.

A. Representative Seahorse XF traces of oxygen consumption rate (OCR) in 6-hr serum starved mHypo43 cells treated with DMSO (control) or STX (1, 5, 10 nM). Sequential injections of oligomycin, FCCP, and rotenone/antimycin A were used to assess mitochondrial respiratory function. **B–G**. Quantification of mitochondrial respiration parameters derived from OCR measurements, including basal respiration (**B**), ATP-linked respiration (**C**), maximal respiration (**D**), spare respiratory capacity (**E**), non-mitochondrial oxygen consumption (**F**), and proton leak (**G**). STX at 1 nM significantly increased basal respiration, ATP-linked respiration, maximal respiration, and spare respiratory capacity compared to control. Similar but less pronounced effects were observed at 5 nM. In contrast, 10 nM STX showed diminished or non-significant effects across most parameters. Proton leak and non-mitochondrial respiration were modestly increased at lower doses but showed no significant differences at higher concentrations. **H**. Representative extracellular acidification rate (ECAR) traces during the glycolysis stress test under the same treatment conditions. Sequential injections of glucose, oligomycin, and 2-deoxyglucose (2-DG) were used to assess glycolytic function. **I–L**. Quantification of glycolytic parameters derived from ECAR measurements, including glycolysis (I), glycolytic capacity (**J**), glycolytic reserve (**K**), and non-glycolytic acidification (**L**). STX at 1 nM and 5 nM significantly increased glycolysis and glycolytic capacity. At 1 nM, STX significantly increased glycolytic reserve and non- glycolytic acidification, with moderate effects observed at 5 nM. In contrast, 10 nM STX did not significantly enhance these parameters, consistent with a non-monotonic dose–response relationship. Data are presented as mean ± SEM with individual data points shown. Statistical significance was determined by one-way ANOVA followed by Dunnett's multiple comparison test. ns-not significant, *p < 0.05, **p < 0.01, ***p < 0.001, ****p < 0.0001.

diazirine-containing BF-STX probe provided a means to covalently stabilize ligand-associated proteins after UV activation (Moellering and Cravatt, 2012; Schultz et al., 2022). The alkyne handle then enabled selective enrichment of BF-STX–labeled proteins through copper-catalyzed azide–alkyne cycloaddition, thereby reducing background and increasing confidence in target identification. Importantly, the use of no-UV controls and competition with excess unlabeled STX strengthened the specificity of the chemoproteomic hits. Therefore, the enrichment of VDAC1–3 under BF-STX labeling conditions, together with loss of signal after STX competition, supports the conclusion that VDACs are *bona fide* intracellular STX-interacting proteins rather than nonspecific contaminants. Thus, the flash-and-click approach provided a mechanistic bridge between the known cellular actions of STX (Lee et al., 2025) and the subsequent functional validation of VDAC2 gating and mitochondrial bioenergetics.

Given the abundant evidence that mitochondrial dysfunction plays a role in many neurodegenerative diseases (Ashleigh et al., 2023; DAlessandro et al., 2025), the current results are congruent with previous findings that STX is neuroprotective against β-amyloid toxicity both in neuronal cultures and transgenic mouse models of Alzheimer's disease, in part by supporting mitochondrial function and synaptic integrity (Gray et al., 2016; Quinn et al., 2022; Lee et al., 2025). Conversely, the loss of mitochondrial function is clearly involved in neuronal dysfunction throughout the course of AD (Ashleigh et al., 2023; DAlessandro et al., 2025). Hence, our results suggest that the neuroprotective effects of STX likely include the regulation of VDAC function in both the healthy and diseased brain. Interestingly, *Vdac2* was the most highly expressed isoform in POMC neurons, unlike the dominance of VDAC1 expression in most tissues with the exception of the testes and ovaries (Zinghirino et al., 2021). Therefore, we investigated the interaction of STX with VDAC2 using single-channel electrophysiological recordings to determine how nanomolar concentrations of STX affect the VDAC2 channel properties. In these experiments, we reconstituted VDAC2 channels in planar lipid membranes and analyzed their voltage-gating behavior, which is characterized by transitions between open and low-conducting, or closed states, in a voltage-dependent manner, a common feature of all VDAC isoforms (Queralt-Martín et al., 2020; Rosencrans et al., 2025). Nanomolar concentrations of STX increased the voltage sensitivity of VDAC2, reducing the characteristic gating voltage by about 40 mV, as observed upon the application of voltage ramps. Furthermore, in multi-channel recordings, STX enhanced voltage-dependent gating in a concentration-dependent manner with a K_d similar to its potent effects on POMC neurons *ex vivo* (Qiu et al., 2006). These results contrast with the neurosteroid allopregnanolone, which is a potent allosteric modulator of $GABA_A$ channel gating (Majewska et al., 1986; Lambert et al., 1995). Although allopregnanolone can also bind to VDACs, based on photoaffinity labeling, it does not affect their gating properties (Cheng et al., 2019). The present results indicate that STX can function as a potent enhancer of VDAC gating, independent of other protein interactions. Moreover, the STX-induced shift of ion selectivity of VDAC2 closed states towards anions further confirms a direct STX-VDAC2 interaction. The absence of measurable effects on VDAC2 open state conductance or selectivity suggests that the hydrophobic STX interacts with VDAC2 at the protein-lipid interface (Rostovtseva et al., 2020; Rovini et al., 2020).

We also investigated the effects of STX on mitochondrial physiology using mHypo43 POMC cells, which were used for the photo-affinity labeling experiments, and IHH cells, which have been established as an effective assay for mitochondrial function (Lim et al., 2008). Hepatocytes exhibit the highest mitochondrial density within the human body (Xu et al., 2023). Based on the K_d values obtained from our biophysical measurements of channel gating, we evaluated the effects of nanomolar concentrations of STX on mitochondrial respiration and glycolytic function in both cell lines. Notably, we observed the types of changes expected following administration of agents targeting the electron transport chain (*e.g.*, oligomycin); specifically, STX (1 nM) was able to potently increase not only basal respiration but spare respiratory capacity, ATP production and proton leak, which helps maintain $\Delta\psi_m$, and non-mitochondrial respiration in both cell lines. Importantly, STX also increased glycolytic function in the mHypo43 POMC neural cell line, which is congruent with the fact that neurons require glucose uptake and glycolysis to support their high energy needs (Li et al., 2023). STX was equally effective in both serum-free conditions, which

eliminates endogenous estrogens, and media that included serum. These results suggest that STX is more potent than E2 in its ability to enhance mitochondrial respiratory activity and affect VDAC gating through its direct interaction, as suggested by their prominent photo-affinity labeling with BF-STX.

In general, the effects of E2 on mitochondrial function are thought to be transduced via estrogen receptors α and β (ERα, ERβ), which regulate transcriptional responses to enhance the efficiency of respiratory chain complexes and improve ATP synthesis capacity (Simpkins et al., 2008; Huang et al., 2025). Immunoreactive ERα and ERβ have been identified within mitochondria (Simpkins et al., 2008; Klinge, 2020), which is consistent with the supposition that many if not all of the actions of E2 are transcriptionally mediated. E2 activates mitochondrial biogenesis, inhibits the accumulation of reactive oxygen species (ROS), and stabilizes the mitochondrial membrane potential (Klinge, 2020). STX, in contrast, does not bind to ERα or ERβ (Qiu et al., 2003), and its effects at both the plasma membrane and mitochondrial membrane are more rapid (<15 min) than a transcriptionally mediated response (Qiu et al., 2003; Smith et al., 2013; Conde et al., 2016). Most importantly, STX directly modulates VDAC gating in the absence of any transcription factors. Notably, STX potently (1 nM) increased both basal and stress-induced (spare capacity) oxidative phosphorylation in mHypo43 and IHH cells, whereas E2 has not been found to affect basal respiration in mammalian cells (Simpkins et al., 2008).

Ultimately, there are dramatic changes in brain oxidative metabolism during menopause that can promote AD (Brinton et al., 2015; Mosconi et al., 2018). In neuroblastoma cell models and primary hippocampal neuronal cultures, STX protects against Aβ-associated mitochondrial dysfunction and synaptic loss (Gray et al., 2016). Moreover, Quinn and colleagues have shown that STX treatment reduces Aβ burden in 5XFAD (AD) mice treated from 6 to 8 months of life (Quinn et al., 2022), during which time amyloid pathology becomes increasingly pronounced in 5XFAD mice (Oakley et al., 2006; Kimura and Ohno, 2009). STX does not alter the expression of Amyloid Precursor Protein (APP) or Aβ aggregation; however, it can indirectly modulate Aβ production by supporting mitochondrial function, which in turn would mitigate the accumulation of reactive oxygen species that promote amyloidogenic processing of APP to generate Aβ peptides (Tong et al., 2005; Jo et al., 2010). Indeed, our findings in mHypo43 cells and human hepatocytes support the role of STX to enhance mitochondrial respiration. By supporting mitochondrial function, STX might also augment the normal phagocytosis and clearance of pathogenic Aβ, which is similar to actions of insulin and other therapies that have Aβ-lowering effects in the absence of any direct effect on Aβ production (Logan et al., 2018; Matthews et al., 2019).

Material and methods

Animals

All the animal procedures described in this study were performed in accordance with institutional guidelines based on National Institutes of Health standards and approved by the Institutional Animal Care and Use Committee at Oregon Health and Science University (IACUC Protocol TR03-IP00000585).

Pomc^{EGFP} (*RRID:IMSR_JAX:009593*, strain of origin: C57BL/6 J) (Cowley et al., 2001) mice were used. All animals were maintained under controlled temperature and photoperiod (lights on at 0600 h and off at 1800 h) and given free access to food and water.

mHypo43 (mHypoE-N43/5) cells

The embryonic mouse hypothalamus cell line N43/5 (mHypoE-N43/5) was obtained from Cellutions Biosystems (Cedarlane, cat. no. CLU127) and cultured according to the supplier's protocol. Cells were grown in 10 cm tissue culture dishes at 37 °C in 5% CO_2 using DMEM (Gibco, cat. no. 11960-044) containing 4.5 mg/mL D-glucose, supplemented with 2 mM L-glutamine (Sigma-Aldrich, cat. no. G7513), 1× non-essential amino acids (Gibco, cat. no. 11140-050), 1% penicillin/streptomycin

(Sigma-Aldrich, cat. no. P4333), and 10% FBS. Freshly thawed cells were initially seeded and allowed to attach for 4–6 h before medium replacement. Cells were passaged at 70–90% confluence using trypsin and split at ratios between 1:5 and 1:10.

Synthesis and physiological validation of BF-STX probe

The novel bifunctional STX derivative (BF-STX) containing both a photo-cross-linkable diazirine group and an alkyne handle was designed by the Schultz Lab and synthesized in collaboration with SiChem GmbH (Germany) (Figure 1A and see Supplementary Files). To demonstrate that this construct was functional, we tested the efficacy of BF-STX to modulate the excitability of POMC neurons in *ex vivo* electrophysiological slice experiments. Indeed, BF-STX was as efficacious as STX in increasing POMC cell excitability (Qiu et al., 2003; Qiu et al., 2006) (Figure 1B).

Confocal imaging of BF-STX labelling in brain slices

Coronal hypothalamic arcuate slices (250 µm thick) containing POMC neurons were incubated with 10 µM BF-STX for 30 min, then subjected to UV photo-crosslinking (2.5 min, 1000 W Xe lamp with a 350 nm high-pass filter). Slices were fixed in cold methanol (–20 °C, 20 min), and BF-STX–protein conjugates were visualized by Cu(I)-catalyzed click chemistry using Alexa Fluor 488 picolyl azide. Nuclei were counterstained with DAPI. Imaging was performed on an Olympus FV1200 confocal microscope with a 60× oil-immersion objective, using the third ventricle (3V) as an anatomical landmark (Figure 1C).

Confocal Imaging of BF-STX labelling in mHypo43 cells

mHypo43 (POMC neurons) were treated with 10 µM BF-STX for 30 min, followed by UV crosslinking under the same conditions (2.5 min, 1000 W Xe lamp, 350 nm filter) (Figure 1D). After fixation in cold methanol (–20 °C, 20 min), cells were labeled with Alexa Fluor 488 picolyl azide and counterstained with DAPI. Confocal imaging (Olympus FV1200, 60× oil objective) showed robust intracellular accumulation of BF-STX in mHypo43 and MIN6 cells, whereas HeLa Kyoto cells (*RRID:CVCL_1922*) displayed little to no detectable signal.

Visualized whole-cell patch recording

Whole-cell current clamp and voltage clamp recordings were made from POMC neurons as previously described (Qiu et al., 2010; Qiu et al., 2014). Coronal arcuate slices (250 µm) were prepared from gonadectomized females, 10 weeks and older as previously described (Qiu et al., 2010; Qiu et al., 2014). The slices were then transferred to an auxiliary chamber in which they were kept at room temperature (25 °C) in artificial CSF (aCSF) consisting of the following (in mm): 124 NaCl, 5 KCl, 2.6 NaH_2PO_4, 2 $MgSO_4$, 2 $CaCl_2$, 26 $NaHCO_3$, 10 HEPES, 10 glucose, pH 7.4, until recording (recovery for 2 h). A single slice was transferred to the recording chamber at a time and was kept viable by continually perfusing with warm (35 °C), oxygenated aCSF at 1.25 ml/min. Whole-cell patch recordings were made from POMC neurons using an Olympus BX51 W1 fixed stage scope out-fitted with epifluorescence and infrared-differential interference contrast (IR-DIC) video microscopy. Patch pipettes (A-M Systems; 1.5 µm outer diameter borosilicate glass) were pulled on a Brown/Flaming puller (Sutter Instrument, model P-97) and filled with the following solution: 128 mM potassium gluconate, 10 mM NaCl, 1 mM $MgCl_2$, 11 mM EGTA, 10 mM HEPES, 3 mM ATP, and 0.25 mM GTP adjusted to pH 7.3 with KOH; 295 mOsm. Pipette resistances ranged from 3.5 to 4 MΩ. In whole-cell configuration, access resistance was less than 30 MΩ; the access resistance was 80% compensated. The input resistance was calculated by measuring the slope of the I–V relationship curve between −70 and −50 mV. Standard whole-cell patch recording procedures and pharmacological testing were performed as previously described (Qiu et al., 2010). Electrophysiological signals were digitized with a Digidata 1322 A (Axon Instruments) and the data were analyzed using p-Clamp software (Molecular Devices, Foster City, CA).

To study the effect of BF-STX on µ-opioid receptor-mediated responses in POMC neurons, a drug administration protocol was employed during whole-cell patch-clamp recordings in voltage-clamp mode (V_{hold} = –60 mV). After forming a gigaseal and achieving the whole-cell configuration, slices were perfused with tetrodotoxin (TTX, 1 µM) for 5 minutes in order to synaptically isolate the

neurons. The μ-opioid receptor receptor-mediated response was evoked by perfusing [D-Ala2, N-MePhe4, Gly-ol]-enkephalin (DAMGO, 300 nM) until a steady-state outward current was reached. Following drug washout, the current returned to its pre-drug baseline. Cells were then treated with BF-STX for 15 minutes. DAMGO was perfused again, and the second response was recorded.

A standard artificial cerebrospinal fluid was used (Qiu et al., 2010). TTX (1 mM, Alomone Labs) and DAMGO (1 mM, d-Ala2, N-Me-Phe4, Gly-ol5-enkephalin; Peninsula Laboratories, Inc., Belmont, CA) were dissolved in H_2O. BF-STX (10 mM) was dissolved in 100% ethanol. Aliquots of the stock solution was stored as appropriate until needed.

Identification of candidate STX targets in POMC neurons using BF-STX

mHypo43 cells (3 x 10^6 cells) were grown in culture medium (see above) and incubated with 10 μM BF-STX in DMEM for 5 min or 30 min. Photo-crosslinking was performed for 5 min. BF-STX without UV crosslinking and pre-incubation with STX before cross-linking served as negative controls. After washing and scraping, cells were lysed on ice by probe sonication (three 15 s bursts). Lysates were subjected to copper-catalyzed azide–alkyne cycloaddition (CuAAC) with picolyl azide agarose beads for selective enrichment of labeled proteins. Azide beads (200 μL) were washed in deionized water, added to lysate with $CuSO_4$ (1 mM), sodium ascorbate (1 mM), and TBTA (100 μM), and incubated at room temperature for 1 h with rotation. Beads were pelleted (1000 x g, 2 min), transferred to centrifuge columns, and washed with PBS (3×), bead wash buffer 1 (100 mM Tris-HCl, pH 8.0, 250 mM NaCl, 5 mM EDTA, 1% SDS; 5×), and bead wash buffer 2 (100 mM Tris-HCl, pH 8.0, 8 M urea; 10×). Beads were transferred to clean tubes and pelleted.

Captured proteins were reduced in digestion buffer (100 mM Tris-HCl, pH 8.0, 2 mM $CaCl_2$, 10% acetonitrile) with DTT (10 mM) at 42 °C for 30 min and alkylated with iodoacetamide (40 mM) at room temperature in the dark for 30 min. Bead-bound proteins were digested overnight at 37 °C with sequencing-grade trypsin. Peptides were desalted on C18 cartridges and stored at −80 °C prior to shipping to EMBL.

Identification of isolated proteins by LC-MS/MS (see Supplementary Files for complete protocol

Up to 10 μg of peptides were labeled using TMTpro™ 16plex reagent as previously described (Thompson et al., 2019). Briefly, 0.5 mg of TMT reagent was dissolved in 45 μL of 100% acetonitrile. Subsequently, 4 μL of this solution was added to each peptide sample, followed by incubation at room temperature for 1 hour. The labeling reaction was quenched by adding 4 μL of a 5% aqueous hydroxylamine solution and incubating for an additional 15 minutes at room temperature. Labeled samples were then combined for multiplexing, desalted using an Oasis® HLB μElution Plate (Waters) according to the manufacturer's instructions, and dried by vacuum centrifugation.

Peptides were separated on an UltiMate 3000 RSLCnano system using a C18 trapping cartridge (μ-Precolumn PepMap™ 100, 300 μm × 5 mm, 5 μm, 100 Å) and an analytical column (nanoEase™ M/Z HSS T3, 75 μm × 250 mm, 1.8 μm, 100 Å). Samples were trapped at 30 μL/min in 0.05% TFA for 6 min and then gradient-eluted at 0.3 μL/min with solvent A (3% DMSO, 0.1% formic acid in water) and solvent B (3% DMSO, 0.1% formic acid in acetonitrile): 2–8% B (4 min), 8–26% B (104 min), 26–38% B (4 min), 40–80% B (0.1 min), 80% B (3.9 min), followed by re-equilibration to 2% B (4 min).

Peptides were analyzed on an Orbitrap Fusion™ Lumos™ Tribrid™ mass spectrometer in positive ion mode with a Pico-Tip nanospray emitter (2.2 kV spray voltage, capillary temperature 275 °C). Full MS scans (m/z 375–1500) were acquired in the Orbitrap at 120 000 resolution with a maximum injection time of 50 ms. Data-dependent MS/MS spectra were acquired at 30 000 resolution with a maximum injection time of 94 ms and AGC target of 200%. HCD fragmentation was used with normalized collision energy of 34%, a quadrupole isolation window of 0.7 m/z, and dynamic exclusion of 60 s; precursor charge states 2–7 were selected for fragmentation.

Data analysis

Raw files were converted to mzML format using MSConvert (ProteoWizard, *RRID:SCR_012056*) with peak picking and zlib compression. Spectra were searched with MSFragger in FragPipe (v19.0) against the UniProt (*RRID:SCR_002380*) Homo sapiens reference proteome (UP000005640) including common contaminants and reversed sequences. Carbamidomethylation (C, 57.0215) and TMTpro (K, 304.2072) were set as fixed modifications; oxidation (M, 15.9949), protein N-terminal acetylation (42.0106), and TMTpro (peptide N-terminus, 304.2072) were included as variable modifications. Trypsin specificity with up to two missed cleavages and a minimum peptide length of seven residues was used; precursor and fragment mass tolerances were set to 20 ppm; peptide and protein FDR were controlled at 1% using standard FragPipe settings.

FragPipe (protein.tsv files) were processed using the R programming environment (ISBN 3-900051-07-0). Initial data processing included filtering out contaminants and reverse proteins. Only proteins quantified with at least 2 unique peptides (Unique.Peptides >= 2) were considered for further analysis. 878 proteins passed the quality control filters. In order to correct for technical variability, batch effects were removed using the 'removeBatchEffect' function of the limma (*RRID:SCR_010943*) package (Ritchie et al., 2015) on the log2 transformed raw TMT reporter ion intensities ('channel' columns). Subsequently, normalization was performed using the 'normalizeVSN' function of the limma package (VSN - variance stabilization normalization – (Huber et al., 2002)). For visualization, proteins abundances were normalized to the control condition by dividing by the median of control replicates ('ctrl' column). These control ratios were used for clustering and heatmap display. Differential expression analysis was performed using the moderated t-test provided by the limma package (Ritchie et al., 2015). The model accounted for replicate information by including it as a factor in the design matrix passed to the 'lmFit' function. To obtain p-values and false discovery rates (FDRs), the 'fdrtool' function from the fdrtool package (Strimmer, 2008) was used to analyze the t-values produced by limma for certain comparisons. Proteins were annotated as hits if they had a false discovery rate (FDR) below 0.05 and an absolute fold change greater than 2. Proteins were considered candidates if they had an FDR below 0.2 and an absolute fold change greater than 1.5. Clustering based on the median protein abundances normalized by median of control condition was conducted to identify groups of proteins with similar patterns across conditions. The 'kmeans' method was employed, using Euclidean distance as the distance metric and 'ward.D2' linkage for hierarchical clustering. The optimal number of clusters (6) was determined using a hybrid Silhouette approach. The threshold was set as the maximum of either the 80th percentile of silhouette values or a fixed floor of 0.25 (threshold = 0.403), selecting the maximum number of clusters exceeding this threshold. This hybrid approach balances data-driven cluster selection while avoiding selection from noisy low-quality regions.

Cell harvesting of dispersed and POMC neurons and quantitative real-time PCR (qPCR)

Cell harvesting and qPCR was conducted as previously described (Bosch et al., 2013). The ARH was microdissected from basal hypothalamic coronal slices obtained from female $Pomc^{EGFP}$ mice in which POMC neurons were labeled with YFP (n = 3 animals/group). The dispersed cells were visualized, patched, and then harvested (10 cells/tube) as described previously (Bosch et al., 2013). Briefly, the tissue was incubated in papain (7 mg/ml in oxygenated aCSF) for 50 min at 37°C and washed 4 times in low Ca^{2+} aCSF and two times in aCSF. Gentle trituration with Pasteur pipettes were used to disperse the neurons onto a glass bottom dish. Oxygenated aCSF circulated into the plate keeping the cells clear of debris. Only healthy cells with processes and a smooth cell membrane were harvested. The cells were harvested using the XenoWorks Microinjector System (Sutter Instruments, Navato, CA), which provided negative pressure in the pipette and fine control to draw the cell up into the pipette. Cells were harvested as pools of 10 individual cells/tube.

Primers for the genes that encode for *Vdac1*, *Vdac2*, *Vdac3* and *β-actin* were designed using Clone Manager software (Sci Ed Software) (*RRID:SCR_014521*) to cross at least one intron-exon boundary and optimized as previously described using Power SYBR Green method (Bosch et al.,

2013; Nestor et al., 2016). We have published previously the primers for *β-actin* (Qiu et al., 2018), which have similar efficiency as the *Vdac* primers (see Table1). Controls included neuronal pools reacted without reverse transcriptase (RT), hypothalamic RNA reacted with RT and without RT, as well as water blanks. Primers (Table 1) for qPCR were further tested for efficiency ($E = 10^{(-1/m)} - 1$) (Livak and Schmittgen, 2001; Pfaffl, 2001; Bosch et al., 2013).

qPCR was performed on a Quantstudio 7 Flex Real-Time PCR System (Life Technologies) using Power SYBR Green (Life Technologies) Master Mix according to established protocols (Bosch et al., 2013). The comparative $\Delta\Delta C_T$ method (Livak and Schmittgen, 2001; Pfaffl, 2001) was used to determine values from duplicate samples of 4 µl for the target genes and 2 µl for the reference gene β-actin in a 20 µl reaction volume containing 1× Power SYBR Green PCR Master Mix (Applied Biosystems) and 0.5 µM forward and reverse primers. Three 10 cell neuronal pools/animal (n=3 animals) were used to determine the relative linear quantity using the $2^{-\Delta\Delta CT}$ equation (Bosch et al., 2013). In order to compare the relative expression levels of target genes *Vdac1*, *Vdac2* and *Vdac3* in $POMC^{EGFP}$ neurons the mean Δ CT for target gene *Vdac2* was used as the calibrator.

Measurements of VDAC activity in planar lipid membranes

Planar lipid bilayers were made by the apposition of two monolayers comprised of the 1:1 (w:w) mixture of dioleoyl-phosphatidylcholine (DOPC) and dioleoyl-phosphatidylethanolamine (DOPE) lipids (1:1 w/w) or diphytanoyl-phosphatidylcholine (DPhPC) (Avanti Polar Lipids, Alabaster, AL) dissolved in pentane. These bilayers were formed across a ~125 µm (in multichannel experiments) and 75 µm (in single-channel experiments) diameter aperture in the 15-µm-thick Teflon partition separating two ~1.5-mL compartments, as previously described (Rostovtseva et al., 2006). The recombinant human VDAC2 was a generous gift of Tsyr-Yan Dharma Yu (Institute of Atomic and Molecular Sciences, Academia Sinica, Taipei, Taiwan). VDAC2 channel insertion was achieved by the addition of 0.2-0.5 µl of VDAC2 diluted in 100 mM Tris, 50 mM KCl, 1 mM EDTA, 15% (v/v) DMSO, 2.5% (v/v) Triton X-100, pH 7.35 to the cis (grounded) compartment of the experimental chamber while stirring, as described previously (Rostovtseva et al., 2006; Rostovtseva and Bezrukov, 2015).). Ion current recordings were acquired using an Axopatch 200B amplifier (Axon Instruments) in the voltage clamp mode, following previously reported protocols (Rostovtseva and Bezrukov, 2015). Current signals were filtered at 10 kHz with a low-pass Bessel (8 pole) filter, digitized at a sampling frequency of 50 kHz, and analyzed using pClamp10.7 software (Axon Instruments For single-channel analyses in Clampfit 10.7, recordings were further digitally filtered with a 5 kHz 8-pole Bessel low-pass filter. Potential is defined as positive when it is greater on the cis side, the side of compound STX and VDAC2 addition. STX was added from its stock solution in DMSO.

Voltage dependence of VDAC2 gating was analyzed using a previously described protocol (Rostovtseva et al., 2006; Teijido et al., 2014) under the application of a slow, symmetric triangular voltage wave (±60 mV, 5 mHz) generated by an Arbitrary Waveform Generator 33220A (Agilent Technologies). Data were sampled at 2 Hz frequency and analyzed as detailed earlier (Teijido et al., 2014) using a custom in-house algorithm (Rappaport et al., 2015) and pClamp 10.7 software (*RRID:SCR_011323*). In each experiment, current records were collected from membranes containing more than 20 channels in response to 5–10 periods of voltage waves to ensure data collection from more than 100 channels per experiment. Only the part of the wave, during which the channels were reopening, was used for the subsequent analysis for the reasons described elsewhere (Colombini, 1989; Teijido et al., 2014). G_{min}, the minimal multichannel conductance in multichannel experiments, was measured at applied potentials in the range of 50 mV < |V| < 60 mV.

VDAC selectivity was measured in 1M (cis) / 200mM (trans) KCl gradient buffered with 5 mM HEPES at pH 7.4, as described previously (Teijido et al., 2014). In all experiments, VDAC2 was added to the cis compartment. VDAC2 ion selectivity was calculated from the potential corresponding to the zero current (Ψ_{rev}) using a linear regression fit to the data.

Gene Name (encodes for)	Accession Number	Primer Location (nt)	Product Length (bp)	Annealing Temp (°C)	Efficiency Slope	r^2	%
VDAC1	NM_001362693	233-352	120	60	-3.445	0.86	95
VDAC2	NM_011695	192-266	77	60	-3.567	0.99	93
VDAC3	NM_00119898	905-987	83	60	-3.507	0.99	91
β-Actin	NM_007393	446-555	110	60	-3.465	0.99	95

Table 1. Primer Table

Flow cytometry assay

mHypo43 cells were seeded in 24-well plates at $1x10^5$ cells/well and incubated overnight in serum-free DMEM without phenol red in the presence of 50 nM or 100 nM STX. 1 µM LIVE/DEAD™ Fixable Near-IR Dead Cell stain (Thermo Fisher Scientific, L34976) was added to each sample and the fluorescence was measured by exciting cells with 637 nm laser and detecting emission with 780/60 nm bandpass filter. Labeled cells were acquired on a flow cytometer (BD FACSymphony A5) with FACSDiva software v9.3.1(*RRID:SCR_001456*). Analysis was performed in FlowJo v10.10 (*RRID:SCR_008520*) with gating on singlet live cells, and the geometric mean for label fluorescence was determined for each condition.

Mitochondrial membrane potential

Cells were trypsinized and incubated with 5nM TMRM (Tetramethylrhodamine methyl ester, Thermo Fisher Scientific, M20036) and LIVE/DEAD™ Fixable Near-IR Dead Cell stain in PBS for 30 mins at 37 °C in a 5% CO_2 incubator. Cells were washed and resuspended in 250 µL PBS and acquired on low speed. The fluorescence of TMRM was measured by exciting the cells with a 561 nm laser, and the emission was detected with bandpass filter of 586/15 nm.

Mitochondrial calcium

Cells were trypsinized and incubated with 2 µM Rhod2-AM (Thermo Fisher Scientific, R1245MP) and 0.02% Pluronic® F-127 (Sigma-Aldrich, P2443) in PBS for 45 mins at room temperature. Cells were washed and incubated with LIVE/DEAD™ Fixable Near-IR Dead Cell stain in 250 µL PBS for 30 mins at room temperature and acquired on low speed. The fluorescence of Rhod2 was measured by exciting the cells with a 561 nm laser, and the emission was detected with bandpass filter of 586/15 nm.

Mitochondrial ATP

Cells were trypsinized and incubated with 5 µM Biotracker ATP-Red (Sigma-Aldrich, SCT045) and LIVE/DEAD™ Fixable Near-IR Dead Cell stain in PBS for 15 mins at 37 °C and 5% CO_2. Cells were washed and resuspended in 250 µL PBS and acquired on low speed. The fluorescence of ATP-Red was measured by exciting cells with a 561 nm laser, and the emission was detected with a bandpass filter of 586/15 nm.

Seahorse Assays

Cellular bioenergetics were assessed using the Seahorse XFe96 Analyzer (Agilent Technologies) with either the XF Cell Mito Stress Test Kit (Agilent Technologies, 103015-100) or the XF Glycolysis Stress Test Kit (Agilent Technologies, 103020-100), following the manufacturer's protocols. Seahorse XFe 96-well plates (Agilent Technologies, 103794-100) were coated with rat tail collagen type I (Gibco, A10483-01) for 1 h at room temperature, air-dried under sterile conditions, and seeded with immortalized human hepatocytes (IHH) or mHypo43 cells at 20,000 cells per well, followed by overnight incubation at 37°C with 5% CO_2. The Seahorse XFe96 sensor cartridge (Agilent Technologies, W11425) was hydrated overnight in Seahorse XF Calibrant (Agilent Technologies, 100840-000) at 37°C in a non-CO_2 incubator. On the day of each assay, cells were washed twice with Dulbecco's phosphate-buffered saline (Gibco, 14190-144), serum-starved for 6 h, and then washed twice with Seahorse XF DMEM medium, pH 7.4 (Agilent Technologies, 103575-100). Cells were incubated for 1 h at 37°C in a non-CO_2 incubator with either 1 nM STX, 5nM STX (for mHypo43 cells), 10 nM STX, or Seahorse XF assay medium alone (control) immediately prior to the assay. To assess the impact of serum starvation, additional assays were performed in the same manner but without the 6 h serum starvation step.

For the Mito Stress Test, the Seahorse assay medium was supplemented with 10 mM glucose, 1 mM pyruvate, and 2 mM L-glutamine, and injection ports were loaded with 1.5 µM oligomycin, 1 µM FCCP, and 0.5 µM rotenone/antimycin A. Oxygen consumption rate (OCR) was measured in real

time using cycles of mixing (3 min), waiting (2 min), and measuring (3 min), and basal respiration, ATP-linked respiration, maximal respiration, spare respiratory capacity, and non-mitochondrial respiration were calculated.

For the Glycolysis Stress Test, the Seahorse assay medium was supplemented with 2 mM L-glutamine only, and injection ports were loaded with 10 mM glucose, 1 µM oligomycin, and 50 mM 2-deoxy-D-glucose (2-DG).

Extracellular acidification rate (ECAR) was measured using the same cycle parameters described above, and glycolysis, glycolytic capacity, glycolytic reserve, and non-glycolytic acidification were calculated. All data were analyzed using Wave software (Agilent Technologies). Each treatment group was assayed in at least eight technical replicates per plate, and all experiments were independently repeated a minimum of three times. Wells with poor adherence or OCR/ECAR values exceeding two standard deviations from the mean were excluded from analysis.

Data are presented as mean ± standard error (SE). Statistical significance was determined using one-way ANOVA followed by Dunnett's multiple comparison test.

Data availability

All data generated or analyzed during this study are included in the manuscript and supporting files. Source data files have been provided for all figures. Additional data and analysis code are available from the corresponding author upon reasonable request.

Acknowledgements

The authors would like to thank Jin Hui-Deng for his assistance in breeding and genotyping the transgenic mouse lines at OHSU. The click chemistry, molecular biological and electrophysiological studies were supported by the National Institutes of Health grants: NIA grant R21 AG080057 (MJK & CS) and NIDDK grant R01 DK068098 (MJK & OKR). Research at the Intramural Research Program of the *Eunice Kennedy Shriver* National Institute of Child Health and Human Development, National Institutes of Health was funded by NIH grant ZIA HD000072-18 (SMB). The contributions of the NIH authors (SMB, TKR, MR, MW, WF) are considered Works of the United States Government. The findings and conclusions presented in this paper are those of the authors and do not necessarily reflect the views of the National Institutes of Health or the U.S. Department of Health and Human Services.

Additional files

Supplementary file 1. Additional experimental details, materials, methods and supporting figures, including NMR spectra.

Additional information

Funding

Funder	Grant reference number	Author
National Institute on Aging	R21 AG080057	Carsten Schultz
National Institute of Diabetes and Digestive and Kidney Diseases	R01 DK068098	Oline K Rønnekleiv
National Institutes of Health	ZIA HD000072-18	Sergey Bezrukov

Author ORCID iDs

Jian Qiu: https://orcid.org/0000-0002-4988-8587
Oline K Rønnekleiv: https://orcid.org/0000-0003-1841-4386
Carsten Schultz: https://orcid.org/0000-0002-5824-2171
Martin J Kelly: https://orcid.org/0000-0002-8633-2510

References

Ashleigh T, Swerdlow RH, Beal MF (2023) The role of mitochondrial dysfunction in Alzheimer's disease pathogenesis. *Alzheimers Dement* **19**:333-342 https://doi.org/10.1002/alz.12683 | PubMed

Bosch MA, Tonsfeldt KJ, Rønnekleiv OK (2013) mRNA expression of ion channels in GnRH neurons: subtype-specific regulation by 17β-Estradiol. *Molecular and Cellular Endocrinology* **367**:85-97 https://doi.org/10.1016/j.mce.2012.12.021 | PubMed

Brinton RD, Yao J, Yin F, Mack WJ, Cadenas E (2015) Perimenopause as a neurological transition state. *Nature Reviews Endocrinology* **11**:393 https://doi.org/10.1038/nrendo.2015.82 | PubMed

Camara AKS, Zhou Y, Wen PC, Tajkhorshid E, Kwok WM (2017) Mitochondrial VDAC1: A Key Gatekeeper as Potential Therapeutic Target. *Front Physiol* **8**:460 https://doi.org/10.3389/fphys.2017.00460 | PubMed

Cheng WWL, Budelier MM, Sugasawa Y, Bergdoll L, Queralt-Martín M, Rosencrans W, Rostovtseva TK, Chen ZW, Abramson J, Krishnan K, *et al.* (2019) Multiple neurosteroid and cholesterol binding sites in voltage-dependent anion channel-1 determined by photo-affinity labeling. *Biochim Biophys Acta Mol Cell Biol Lipids* **1864**:1269-1279 https://doi.org/10.1016/j.bbalip.2019.06.004 | PubMed

Colombini M (1989) Voltage gating in the mitochondrial channel, VDAC. *J Membr Biol* **111**:103-111 https://doi.org/10.1007/bf01871775 | PubMed

Colombini M (2004) VDAC: the channel at the interface between mitochondria and the cytosol. *Mol Cell Biochem* **256-257**:107-115 https://doi.org/10.1023/b:mcbi.0000009862.17396.8d | PubMed

Conde K, Meza C, Kelly MJ, Sinchak K, Wagner EJ (2016) Estradiol Rapidly Attenuates ORL-1 Receptor-Mediated Inhibition of Proopiomelanocortin Neurons via G_q-Coupled, Membrane-Initiated Signalling. *Neuroendocrinology* **103**:787-805 https://doi.org/10.1159/000443765 | PubMed

Cowley MA, Smart JL, Rubinstein M, Cerdán MG, Diano S, Horvath TL, Cone RD, Low MJ (2001) Leptin activates anorexigenic POMC neurons through a neural network in arcuate nucleus. *Nature* **411**:480-484 https://doi.org/10.1038/35078085 | PubMed

DAlessandro MCB, Kanaan S, Geller M, Praticò D, Daher JPL (2025) Mitochondrial dysfunction in Alzheimer's disease. *Ageing Res Rev* **107**:102713 https://doi.org/10.1016/j.arr.2025.102713 | PubMed

Divakaruni AS, Paradyse A, Ferrick DA, Murphy AN, Jastroch M (2014) Analysis and interpretation of microplate-based oxygen consumption and pH data. *Methods Enzymol* **547**:309-354 https://doi.org/10.1016/b978-0-12-801415-8.00016-3 | PubMed

Gray NE, Zweig JA, Kawamoto C, Quinn JF, Copenhaver PF (2016) STX, a novel membrane estrogen receptor ligand, protects against amyloid-β toxicity. *J Alzheimers Dis* **51**:391-403 https://doi.org/10.3233/jad-150756 | PubMed

Haberkant P, Raijmakers R, Wildwater M, Sachsenheimer T, Brügger B, Maeda K, Houweling M, Gavin A-C, Schultz C, van Meer G, *et al.* (2013) In Vivo Profiling and Visualization of Cellular Protein–Lipid Interactions Using Bifunctional Fatty Acids. *Angewandte Chemie International Edition* **52**:4033-4038 https://doi.org/10.1002/anie.201210178 | PubMed

Höglinger D, Nadler A, Haberkant P, Kirkpatrick J, Schifferer M, Stein F, Hauke S, Porter FD, Schultz C (2017) Trifunctional lipid probes for comprehensive studies of single lipid species in living cells. *Proceedings of the National Academy of Sciences* **114**:1566-1571 https://doi.org/10.1073/pnas.1611096114 | PubMed

Huang X, Pan CH, Yin F, Peng J, Yang L (2025) The Role of Estrogen in Mitochondrial Disease. *Cell Mol Neurobiol* **45**:68 https://doi.org/10.1007/s10571-025-01592-8 | PubMed

Huber W, von Heydebreck A, Sültmann H, Poustka A, Vingron M (2002) Variance stabilization applied to microarray data calibration and to the quantification of differential expression. *Bioinformatics* **18 Suppl 1**:S96-104 https://doi.org/10.1093/bioinformatics/18.suppl_1.s96 | PubMed

Hulce JJ, Cognetta AB, Niphakis MJ, Tully SE, Cravatt BF (2013) Proteome-wide mapping of cholesterol-interacting proteins in mammalian cells. *Nat Methods* **10**:259-264 https://doi.org/10.1038/nmeth.2368 | PubMed

Jo DG, Arumugam TV, Woo HN, Park JS, Tang SC, Mughal M, Hyun DH, Park JH, Choi YH, Gwon AR, *et al.* (2010) Evidence that gamma-secretase mediates oxidative stress-induced beta-secretase expression in Alzheimer's disease. *Neurobiol Aging* **31**:917-925 https://doi.org/10.1016/j.neurobiolaging.2008.07.003 | PubMed

Kimura R, Ohno M (2009) Impairments in remote memory stabilization precede hippocampal synaptic and cognitive failures in 5XFAD Alzheimer mouse model. *Neurobiology of Disease* **33**:229-235 https://doi.org/10.1016/j.nbd.2008.10.006 | PubMed

Kleiner P, Heydenreuter W, Stahl M, Korotkov VS, Sieber SA (2017) A Whole Proteome Inventory of Background Photocrosslinker Binding. *Angew Chem Int Ed Engl* **56**:1396-1401 https://doi.org/10.1002/anie.201605993 | PubMed

Klinge CM (2020) Estrogenic control of mitochondrial function. *Redox Biol* **31**:101435 https://doi.org/10.1016/j.redox.2020.101435 | PubMed

Lambert JJ, Belelli D, Hill-Venning C, Peters JA (1995) Neurosteroids and $GABA_A$ receptor function. *Trends in Pharmacological Sciences* **16**:295-303 https://doi.org/10.1016/s0165-6147(00)89058-6 | PubMed

Lebesgue D, Traub M, De Butte-Smith M, Chen C, Zukin RS, Kelly MJ, Etgen AM (2010) Acute administration of non-classical estrogen receptor agonists attenuates ischemia-induced hippocampal neuron loss in middle-aged female rats. *PLOS One* **5**:e8642 https://doi.org/10.1371/journal.pone.0008642 | PubMed

Lee H-J, Bostick Z, Doherty J, Swanson TL, Kelly MJ, Quinn JF, Gray NE, Copenhaver PF (2025) Neuroprotection against beta-amyloid toxicity by the novel estrogen receptor modulator STX requires convergent signaling pathways. *Frontiers in Molecular Neuroscience* **18**:2025 https://doi.org/10.3389/fnmol.2025.1670646 | PubMed

Li H, Guglielmetti C, Sei YJ, Zilberter M, Le Page LM, Shields L, Yang J, Nguyen K, Tiret B, Gao X, *et al.* (2023) Neurons require glucose uptake and glycolysis in vivo. *Cell Reports* **42**:112335 https://doi.org/10.1016/j.celrep.2023.112335 | PubMed

Lim PL, Liu J, Go ML, Boelsterli UA (2008) The mitochondrial superoxide/thioredoxin-2/Ask1 signaling pathway is critically involved in troglitazone-induced cell injury to human hepatocytes. *Toxicol Sci* **101**:341-349 https://doi.org/10.1093/toxsci/kfm273

Livak KJ, Schmittgen TD (2001) Analysis of relative gene expression data using real-time quantitative PCR and the $2^{-\Delta\Delta CT}$ method. *Methods* **25**:402-408 https://doi.org/10.1006/meth.2001.1262 | PubMed

Logan S, Pharaoh GA, Marlin MC, Masser DR, Matsuzaki S, Wronowski B, Yeganeh A, Parks EE, Premkumar P, Farley JA, *et al.* (2018) Insulin-like growth factor receptor signaling regulates working memory, mitochondrial metabolism, and amyloid-β uptake in astrocytes. *Mol Metab* **9**:141-155 https://doi.org/10.1016/j.molmet.2018.01.013 | PubMed

Majewska MD, Harrison NL, Schwartz RD, Barker JL, Paul SM (1986) Steroid hormone metabolites are barbiturate-like modulators of the GABA receptor. *Science* **232**:1004-1007 https://doi.org/10.1126/science.2422758

Matthews DG, Caruso M, Murchison CF, Zhu JY, Wright KM, Harris CJ, Gray NE, Quinn JF, Soumyanath A (2019) Centella Asiatica Improves Memory and Promotes Antioxidative Signaling in 5XFAD Mice. *Antioxidants* **8** https://doi.org/10.3390/antiox8120630 | PubMed

Moellering RE, Cravatt BF (2012) How chemoproteomics can enable drug discovery and development. *Chem Biol* **19**:11-22 https://doi.org/10.1016/j.chembiol.2012.01.001 | PubMed

Morrison JH, Brinton RD, Schmidt PJ, Gore AC (2006) Estrogen, menopause, and the aging brain: how basic neuroscience can inform hormone therapy in women. *The Journal of Neuroscience* **26**:10332-10348 https://doi.org/10.1523/jneurosci.3369-06.2006 | PubMed

Mosconi L, Rahman A, Diaz I, Wu X, Scheyer O, Hristov HW, Vallabhajosula S, Isaacson RS, de Leon MJ, Brinton RD (2018) Increased Alzheimer's risk during the menopause transition: A 3-year longitudinal brain imaging study. *PLOS One* **13**:e0207885 https://doi.org/10.1371/journal.pone.0207885 | PubMed

Müller R, Citir M, Hauke S, Schultz C (2020) Synthesis and Cellular Labeling of Caged Phosphatidylinositol Derivatives. *Chemistry – A European Journal* **26**:384-389 https://doi.org/10.1002/chem.201903704 | PubMed

Müller R, Kojic A, Citir M, Schultz C (2021) Synthesis and Cellular Labeling of Multifunctional Phosphatidylinositol Bis- and Trisphosphate Derivatives. *Angewandte Chemie International Edition* **60**:19759-19765 https://doi.org/10.1002/anie.202103599 | PubMed

Murphy S, McCullough L, Littleton-Kearney M, Hurn P (2003) Estrogen and selective estrogen receptor modulators: neuroprotection in the Women's Health Initiative era. *Endocrine* **21**:17-26 https://doi.org/10.1385/endo:21:1:17 | PubMed

Nebel RA, Aggarwal NT, Barnes LL, Gallagher A, Goldstein JM, Kantarci K, Mallampalli MP, Mormino EC, Scott L, Yu WH, *et al.* (2018) Understanding the impact of sex and gender in Alzheimer's disease: A call to action. *Alzheimer's & Dementia* **14**:1171-1183 https://doi.org/10.1016/j.jalz.2018.04.008 | PubMed

Nestor CC, Qiu J, Padilla SL, Zhang C, Bosch MA, Fan W, Aicher SA, Palmiter RD, Rønnekleiv OK, Kelly MJ (2016) Optogenetic stimulation of arcuate nucleus Kiss1 neurons reveals a steroid-dependent glutamatergic input to POMC and AgRP neurons in male mice. *Molecular Endocrinology* **30**:630-644 https://doi.org/10.1210/me.2016-1026 | PubMed

Oakley H, Cole SL, Logan S, Maus E, Shao P, Craft J, Guillozet-Bongaarts A, Ohno M, Disterhoft J, Van Eldik L, *et al.* (2006) Intraneuronal β-amyloid aggregates, neurodegeneration, and neuron loss in transgenic mice with five familial Alzheimer's disease mutations: Potential factors in amyloid plaque formation. *The Journal of Neuroscience* **26**:10129-10140 https://doi.org/10.1523/JNEUROSCI.1202-06.2006 | PubMed

Pfaffl MW (2001) A new mathematical model for relative quantification in real-time RT-PCR. *Nucleic Acids Research* **29**:e45 https://doi.org/10.1093/nar/29.9.e45 | PubMed

Qiu J, Fang Y, Rønnekleiv OK, Kelly MJ (2010) Leptin excites proopiomelanocortin neurons via activation of TRPC channels. *The Journal of Neuroscience* **30**:1560-1565 https://doi.org/10.1523/JNEUROSCI.4816-09.2010 | PubMed

Qiu J, Bosch MA, Tobias SC, Grandy DK, Scanlan TS, Rønnekleiv OK, Kelly MJ (2003) Rapid signaling of estrogen in hypothalamic neurons involves a novel G-protein-coupled estrogen receptor that activates protein kinase C. *The Journal of Neuroscience* **23**:9529-9540 https://doi.org/10.1523/JNEUROSCI.23-29-09529.2003 | PubMed

Qiu J, Rivera HM, Bosch MA, Padilla SL, Stincic TL, Palmiter RD, Kelly MJ, Rønnekleiv OK (2018) Estrogenic-dependent glutamatergic neurotransmission from kisspeptin neurons governs feeding circuits in females. *eLife* **7**:e35656 https://doi.org/10.7554/eLife.35656 | PubMed

Qiu J, Zhang C, Borgquist A, Nestor CC, Smith AW, Bosch MA, Ku S, Wagner EJ, Rønnekleiv OK, Kelly MJ (2014) Insulin excites anorexigenic proopiomelanocortin neurons via activation of canonical transient receptor potential channels. *Cell Metabolism* **19**:682-693 https://doi.org/10.1016/j.cmet.2014.03.004 | PubMed

Qiu J, Bosch MA, Tobias SC, Krust A, Graham S, Murphy S, Korach KS, Chambon P, Scanlan TS, Rønnekleiv OK, *et al.* (2006) A G-protein-coupled estrogen receptor is involved in hypothalamic control of energy homeostasis. *The Journal of Neuroscience* **26**:5649-5655 https://doi.org/10.1523/JNEUROSCI.0327-06.2006 | PubMed

Queralt-Martín M, Bergdoll L, Teijido O, Munshi N, Jacobs D, Kuszak AJ, Protchenko O, Reina S, Magrì A, De Pinto V, *et al.* (2020) A lower affinity to cytosolic proteins reveals VDAC3 isoform-specific role in mitochondrial biology. *Journal of General Physiology* **152** https://doi.org/10.1085/jgp.201912501 | PubMed

Quinn JF, Kelly MJ, Harris CJ, Hack W, Gray NE, Kulik V, Bostick Z, Brumbach BH, Copenhaver PF (2022) The novel estrogen receptor modulator STX attenuates Amyloid-β neurotoxicity in the 5XFAD mouse model of Alzheimer's disease. *Neurobiol Dis* **174**:105888 https://doi.org/10.1016/j.nbd.2022.105888 | PubMed

Rapp PR, Morrison JH, Roberts JA (2003) Cyclic estrogen replacement improves cognitive function in aged ovariectomized rhesus monkeys. *The Journal of Neuroscience* **23**:5708-5714 https://doi.org/10.1523/JNEUROSCI.23-13-05708.2003 | PubMed

Rappaport SM, Teijido O, Hoogerheide DP, Rostovtseva TK, Berezhkovskii AM, Bezrukov SM (2015) Conductance hysteresis in the voltage-dependent anion channel. *Eur Biophys J* **44**:465-472 https://doi.org/10.1007/s00249-015-1049-2 | PubMed

Reina S, De Pinto V (2017) Anti-Cancer Compounds Targeted to VDAC: Potential and Perspectives. *Curr Med Chem* **24**:4447-4469 https://doi.org/10.2174/0929867324666170530074039 | PubMed

Ritchie ME, Phipson B, Wu D, Hu Y, Law CW, Shi W, Smyth GK (2015) . limma powers differential expression analyses for RNA-sequencing and microarray studies. *Nucleic Acids Research* **43**:e47-e47 https://doi.org/10.1093/nar/gkv007 | PubMed

Roepke TA, Bosch MA, Rick EA, Lee B, Wagner EJ, Seidlova-Wuttke D, Wuttke W, Scanlan TS, Rønnekleiv OK, Kelly MJ (2010) Contribution of a membrane estrogen receptor to the estrogenic regulation of body temperature and energy homeostasis. *Endocrinology* **151**:4926-4937 https://doi.org/10.1210/en.2010-0573 | PubMed

Rosencrans WM, Khuntia H, Ghahari Larimi M, Mahalakshmi R, Yu TY, Bezrukov SM, Rostovtseva TK (2025) Conformational plasticity of mitochondrial VDAC2 controls the kinetics of its interaction with cytosolic proteins. *Sci Adv* **11**:eadv4410 https://doi.org/10.1126/sciadv.adv4410 | PubMed

Rossouw JE, Anderson GL, Prentice RL, LaCroix AZ, Kooperberg C, Stefanick ML, Jackson RD, Beresford SA, Howard BV, Johnson KC, *et al.* (2002) Risks and benefits of estrogen plus progestin in healthy postmenopausal women: principal results From the Women's Health Initiative randomized controlled trial. *The Journal of the American Medical Association* **288**:321-333 https://doi.org/10.1001/jama.288.3.321

Rostovtseva T, Colombini M (1996) ATP flux is controlled by a voltage-gated channel from the mitochondrial outer membrane. *J Biol Chem* **271**:28006-28008 https://doi.org/10.1074/jbc.271.45.28006 | PubMed

Rostovtseva TK, Bezrukov SM (2008) VDAC regulation: role of cytosolic proteins and mitochondrial lipids. *J Bioenerg Biomembr* **40**:163-170 https://doi.org/10.1007/s10863-008-9145-y | PubMed

Rostovtseva TK, Bezrukov SM (2015) Function and Regulation of Mitochondrial Voltage-Dependent Anion Channel. In: Delcour AH (Ed). *Electrophysiology of Unconventional Channels and Pores* Springer. https://doi.org/10.1007/978-3-319-20149-8_1

Rostovtseva TK, Kazemi N, Weinrich M, Bezrukov SM (2006) Voltage gating of VDAC is regulated by nonlamellar lipids of mitochondrial membranes. *J Biol Chem* **281**:37496-37506 https://doi.org/10.1074/jbc.M602548200

Rostovtseva TK, Queralt-Martín M, Rosencrans WM, Bezrukov SM (2020) Targeting the Multiple Physiologic Roles of VDAC With Steroids and Hydrophobic Drugs. *Frontiers in Physiology* **11** https://doi.org/10.3389/fphys.2020.00446 | PubMed

Rovini A, Gurnev PA, Beilina A, Queralt-Martín M, Rosencrans W, Cookson MR, Bezrukov SM, Rostovtseva TK (2020) Molecular mechanism of olesoxime-mediated neuroprotection through targeting α-synuclein interaction with mitochondrial VDAC. *Cell Mol Life Sci* **77**:3611-3626 https://doi.org/10.1007/s00018-019-03386-w | PubMed

Schultz C, Farley SE, Tafesse FG (2022) "Flash & Click": Multifunctionalized Lipid Derivatives as Tools To Study Viral Infections. *J Am Chem Soc* **144**:13987-13995 https://doi.org/10.1021/jacs.2c02705 | PubMed

Shumaker SA, Legault C, Rapp SR, Thal L, Wallace RB, Ockene JK, Hendrix SL, Jones BN, Assaf AR, Jackson RD, *et al.* (2003) Estrogen plus progestin and the incidence of dementia and mild cognitive impairment in postmenopausal women: the Women's Health Initiative Memory Study: a randomized controlled trial. *The Journal of the American Medical Association* **289**:2651-2662 https://doi.org/10.1001/jama.289.20.2651

Simpkins JW, Yang S-H, Sarkar SN, Pearce V (2008) Estrogen actions on mitochondria-physiological and pathological implications. *Molecular and Cellular Endocrinology* **290**:51-59 https://doi.org/10.1016/j.mce.2008.04.013 | PubMed

Smith AW, Rønnekleiv OK, Kelly MJ (2014) Gq-mER signaling has opposite effects on hypothalamic orexigenic and anorexigenic neurons. *Steroids* **81**:31-35 https://doi.org/10.1016/j.steroids.2013.11.007 | PubMed

Smith AW, Bosch MA, Wagner EJ, Rønnekleiv OK, Kelly MJ (2013) The membrane estrogen receptor ligand STX rapidly enhances GABAergic signaling in NPY/AgRP neurons: Role in mediating the anorexigenic effects of 17β-estradiol. *American Journal of Physiology: Endocrinology and Metabolism* **305**:E632-E640 https://doi.org/10.1152/ajpendo.00281.2013 | PubMed

Strimmer K (2008) . fdrtool: a versatile R package for estimating local and tail area-based false discovery rates. *Bioinformatics* **24**:1461-1462 https://doi.org/10.1093/bioinformatics/btn209 | PubMed

Tan W, Colombini M (2007) VDAC closure increases calcium ion flux. *Biochim Biophys Acta* **1768**:2510-2515 https://doi.org/10.1016/j.bbamem.2007.06.002 | PubMed

Teijido O, Rappaport SM, Chamberlin A, Noskov SY, Aguilella VM, Rostovtseva TK, Bezrukov SM (2014) Acidification asymmetrically affects voltage-dependent anion channel implicating the involvement of salt bridges. *J Biol Chem* **289**:23670-23682 https://doi.org/10.1074/jbc.M114.576314 | PubMed

Thompson A, Wölmer N, Koncarevic S, Selzer S, Böhm G, Legner H, Schmid P, Kienle S, Penning P, Höhle C, *et al.* (2019) TMTpro: Design, Synthesis, and Initial Evaluation of a Proline-Based Isobaric 16-Plex Tandem Mass Tag Reagent Set. *Anal Chem* **91**:15941-15950 https://doi.org/10.1021/acs.analchem.9b04474 | PubMed

Tobias SC, Qiu J, Kelly MJ, Scanlan TS (2006) Synthesis and biological evaluation of SERMs with potent nongenomic estrogenic activity. *ChemMedChem* **1**:565-571 https://doi.org/10.1002/cmdc.200500098 | PubMed

Tong Y, Zhou W, Fung V, Christensen MA, Qing H, Sun X, Song W (2005) Oxidative stress potentiates BACE1 gene expression and Abeta generation. *J Neural Transm* **112**:455-469 https://doi.org/10.1007/s00702-004-0255-3 | PubMed

Unten Y, Murai M, Koshitaka T, Kitao K, Shirai O, Masuya T, Miyoshi H (2022) Comprehensive understanding of multiple actions of anticancer drug tamoxifen in isolated mitochondria. *Biochimica et Biophysica Acta (BBA) - Bioenergetics* **1863**:148520 https://doi.org/10.1016/j.bbabio.2021.148520 | PubMed

West AV, Muncipinto G, Wu HY, Huang AC, Labenski MT, Jones LH, Woo CM (2021) Labeling Preferences of Diazirines with Protein Biomolecules. *J Am Chem Soc* **143**:6691-6700 https://doi.org/10.1021/jacs.1c02509 | PubMed

Xu Y, Chu C, Shi Z, Zhang J (2023) The role of hepatocyte mitochondrial DNA in liver injury. *Biomed Pharmacother* **168**:115692 https://doi.org/10.1016/j.biopha.2023.115692 | PubMed

Zinghirino F, Pappalardo XG, Messina A, Nicosia G, De Pinto V, Guarino F (2021) VDAC Genes Expression and Regulation in Mammals. *Front Physiol* **12**:708695 https://doi.org/10.3389/fphys.2021.708695 | PubMed

Peer reviews

Reviewer #1 (Public review):

Summary:

In this study, Qiu et al. examine the effects of the estrogen mimic STX on mitochondrial function and its interaction with VDAC2 in PMOC neurons.

Strengths:

The authors employ a broad range of molecular, cellular, and chemoproteomic approaches with generally sound methodology.

Weaknesses:

The work suffers from major conceptual and experimental issues that substantially limit its scientific impact.

Major Concerns

(1) Lack of Rationale.

The study provides no justification for investigating sex specific aspects of Alzheimer's disease by focusing on VDAC-mediated mitochondrial dysfunction in PMOC neurons. These hypothalamic neurons are not recognized as early or primary sites of AD vulnerability, making the biological premise unclear.

(2) Weak Link to AD Pathogenesis.

Although mitochondrial dysfunction is well established in AD, the authors do not convincingly demonstrate a mechanistic or pathological connection between VDAC2 and AD. VDACs are not established contributors to AD etiology, and the manuscript does not strengthen this association.

(3) Unclear Relevance to AD Contexts.

While the data support an interaction between STX and VDAC2 affecting mitochondrial parameters (ATP production, membrane potential, glycolysis, respiration) in PMOC neurons, the study does not show whether this mechanism is relevant to mitochondrial dysfunction in AD. No validation is provided in AD-related models or in contexts related to sex specific AD phenotypes.

(4) Interpretation of Competitive Binding Data.

The competitive binding results in Figure S4B are not adequately interpreted. The dose-dependent competition observed for VDAC3 suggests it may be a stronger candidate than VDAC2, yet this possibility is not addressed.

https://doi.org/10.7554/eLife.111731.1.sa1

Reviewer #2 (Public review):

Summary:

STX is a non-steroidal, CNS-selective estrogenic compound with neuroprotective effects in stroke and Alzheimer's disease models, but its molecular target has remained unknown for nearly 20 years. In this study, the authors identify VDAC proteins as the direct mitochondrial

targets of STX using chemoproteomics, single-cell qPCR, electrophysiology, and metabolic flux analyses. They further show that VDAC2 is the primary functional target in female POMC neurons, linking STX-mediated VDAC modulation to enhanced mitochondrial bioenergetics and neuroprotection.

Strengths:

This study is strengthened by its innovative chemoproteomic approach, in which the authors developed a novel bifunctional STX probe (BF-STX) containing a photo-crosslinkable diazirine group and an alkyne handle to capture transient STX-protein interactions in living cells. The experimental design is further reinforced by rigorous controls, including no-UV negative controls and competition assays with excess unlabeled STX, which provide convincing evidence that VDAC1, VDAC2, and VDAC3 are genuine STX-binding targets rather than nonspecific artifacts. Finally, the authors validate the STX-VDAC interaction using multiple complementary approaches, including chemoproteomics, single-cell qPCR, planar lipid membrane electrophysiology, and Seahorse metabolic flux analyses, providing strong mechanistic support for their conclusions.

Weaknesses:

While the study provides convincing evidence that STX directly modulates VDAC function, several limitations remain. Most experiments were performed in immortalized cell lines rather than primary neurons or in vivo models, limiting their physiological relevance. In addition, the exact structural binding site of STX on VDAC remains unresolved, and no loss-of-function experiments (e.g., VDAC2 knockdown) were performed to establish a direct causal link between VDAC2 and STX's bioenergetic and neuroprotective effects. The non-linear dose-response at higher STX concentrations also requires further investigation.

https://doi.org/10.7554/eLife.111731.1.sa0

Author response:

> ***Reviewer #1:***

We thank Reviewer #1 for the thoughtful critique. We have revised the manuscript to clarify the physiological rationale for the experimental system, the potential relevance of mitochondrial STX–VDAC signaling to neurodegeneration, and the appropriate scope of our conclusions.

> *(1) Lack of Rationale*
>
> *The study provides no justification for investigating sex-specific aspects of Alzheimer's disease by focusing on VDAC-mediated mitochondrial dysfunction in POMC neurons. These hypothalamic neurons are not recognized as early or primary sites of AD vulnerability, making the biological premise unclear.*

We thank the reviewer for raising this important point. We agree that the original manuscript did not sufficiently explain the rationale for using POMC neurons.

Our rationale is primarily physiological rather than disease-specific. POMC neurons are a well-characterized, metabolically sensitive, and estrogen-responsive neuronal population in which membrane-initiated estrogen signaling and the actions of STX have been extensively characterized. They therefore provide a physiologically relevant neuronal system for identifying the molecular mechanisms through which STX regulates mitochondrial function.

The potential relevance to neurodegeneration is supported by evidence that hypothalamic and POMC neuronal function can be disrupted in neurodegenerative disease models. Do and

colleagues (2018) reported hypothalamic neurodegeneration, increased inflammatory and apoptotic markers, and reduced POMC neuronal populations in 3xTg-AD mice and further showed that exercise attenuated hypothalamic apoptosis and restored POMC neuronal populations (Do, Laing et al. 2018). In addition, Shen and colleagues (2016) demonstrated disruption of POMC/MC4R signaling in APP/PS1 mice and showed that restoration of this pathway improved synaptic function (Shen, Tian et al. 2016).

These studies do not establish POMC neurons as a primary site of AD pathology, but they demonstrate that POMC-related neuronal systems can be vulnerable to neurodegenerative processes. This provides a broader biological context for investigating mitochondrial mechanisms in this neuronal population.

There is also a strong physiological rationale for examining estrogen-sensitive mechanisms in POMC neurons. These neurons are established targets of 17β-estradiol and are highly responsive to metabolic and mitochondrial state. STX is a non-steroidal estrogenic compound that activates membrane-initiated estrogen signaling, and our previous studies demonstrated neuroprotective and mitochondrial effects of STX in a neurodegenerative disease model.

Thus, POMC neurons were used because they provide a well-defined estrogen-responsive and metabolically sensitive neuronal population in which STX signaling can be mechanistically investigated—not because we consider them an initiating site of AD pathology.

We have revised the Introduction and Discussion accordingly. The revised manuscript now emphasizes the physiological significance of STX–VDAC signaling for neuronal mitochondrial function and presents its potential relevance to neurodegeneration as an important area for future investigation.

> *(2) Weak Link to AD Pathogenesis*
>
> *Although mitochondrial dysfunction is well established in AD, the authors do not convincingly demonstrate a mechanistic or pathological connection between VDAC2 and AD. VDACs are not established contributors to AD etiology, and the manuscript does not strengthen this association.*

We agree that the present experiments do not establish VDAC2 as an etiological or pathological driver of AD. This was not the objective of the present study.

The primary goal was to identify the molecular target(s) through which STX influences mitochondrial function. Using BF-STX chemoproteomic capture and competition experiments together with single-cell gene-expression analysis, planar lipid membrane electrophysiology, and mitochondrial metabolic analyses, we identify VDAC proteins as mitochondrial targets of STX and demonstrate functional effects of STX on VDAC channel properties and mitochondrial bioenergetics.

Our previous studies demonstrated neuroprotective and mitochondrial effects of STX in the 5xFAD model (Lee, Bostick et al. 2025), providing a neurodegenerative context that motivated the present mechanistic investigation. However, the current findings should not be interpreted as establishing VDAC2 as an AD pathogenic mechanism.

We have revised the manuscript accordingly. The STX–VDAC interaction is now presented principally as a mitochondrial mechanism with potential relevance to neuronal physiology and neurodegeneration. Whether this pathway contributes to the neuroprotective actions of STX in disease models will require direct experimental testing.

> *(3) Unclear Relevance to AD Contexts*
>
> *While the data support an interaction between STX and VDAC2 affecting mitochondrial parameters (ATP production, membrane potential, glycolysis, respiration) in POMC*

> *neurons, the study does not show whether this mechanism is relevant to mitochondrial dysfunction in AD. No validation is provided in AD-related models or in contexts related to sex-specific AD phenotypes.*

We agree that the present experiments do not directly establish the relevance of the STX–VDAC interaction to mitochondrial dysfunction in AD.

The current study was designed to identify and characterize the molecular mechanism underlying the mitochondrial actions of STX, rather than to test this pathway in a specific neurodegenerative disease model. Our findings demonstrate that STX interacts with VDAC proteins, modifies VDAC channel properties, and alters mitochondrial bioenergetics.

The study builds on our previous findings in the 5xFAD model, in which STX reduced amyloid-β-associated pathology and affected mitochondrial function (Lee, Bostick et al. 2025). The identification of VDAC proteins as STX targets therefore provides a mechanistic foundation for future studies examining whether this pathway contributes to neuronal protection under neurodegenerative conditions.

We have revised the Discussion to acknowledge the absence of direct disease-model validation. Future studies using conditional or neuron-specific manipulation of VDAC isoforms will be important for determining the physiological and neuroprotective significance of STX–VDAC signaling *in vivo*.

Accordingly, our conclusions now emphasize what is directly supported by the present experiments: STX interacts with VDAC proteins and modulates VDAC channel function and mitochondrial bioenergetics. The relevance of this mechanism to neurodegenerative disease remains to be established.

> *(4) Interpretation of Competitive Binding Data*
>
> *The competitive binding results in Figure S4B are not adequately interpreted. The dose-dependent competition observed for VDAC3 suggests it may be a stronger candidate than VDAC2, yet this possibility is not addressed.*

We thank the reviewer for highlighting this important point. We agree that the original manuscript placed too much emphasis on VDAC2 based on the chemoproteomic data.

Our chemoproteomic experiments identified VDAC1, VDAC2, and VDAC3 as STX-interacting proteins. Competition with unlabeled STX produced a particularly clear reduction in VDAC3 labeling, including complete loss of the VDAC3 signal at three molar equivalents of unlabeled STX. We therefore agree that VDAC3 represents an important candidate STX target.

We have revised the Results and Discussion so that the competition experiment is no longer interpreted as demonstrating preferential or exclusive binding to VDAC2.

However, the persistence of VDAC1 and VDAC2 labeling may also be influenced by properties of the BF-STX photoprobe as alkyl diazirine probes can preferentially photolabel membrane proteins (Kleiner, Heydenreuter et al. 2017). We now present this only as a possible technical consideration rather than an explanation established by our data.

Our subsequent emphasis on VDAC2 was based on the integration of several observations. Single-cell qPCR demonstrated that *Vdac2* is the predominant transcript in the native POMC neurons examined (revised Figure 3B), with an approximate expression hierarchy of *Vdac2* > *Vdac3* >> *Vdac1*. In addition on a technical note, recombinant VDAC3 is more difficult to reconstitute reliably into artificial membranes because of its lower stability in detergent.

The revised manuscript therefore recognizes all three VDAC isoforms as candidate STX targets but does not claim that VDAC2 is the exclusive or preferential target. Direct

comparisons of STX binding and functional modulation among the three isoforms will be required to establish isoform selectivity.

> ***Reviewer #2:***

We thank Reviewer #2 for the positive assessment of our chemoproteomic strategy and multidisciplinary characterization of the STX–VDAC interaction. We also appreciate the reviewer's identification of important limitations and directions for future investigation.

> *(1) Physiological Relevance of Cell-Line Experiments*
>
> *Most experiments were performed in immortalized cell lines rather than primary neurons or in vivo models, limiting their physiological relevance.*

We agree that the use of immortalized neuronal cell models represents an important limitation.

However, these models provided the cellular material, reproducibility, and experimental control required for chemoproteomic target capture and Seahorse metabolic measurements. Importantly, we complemented these studies with single-cell analysis of native POMC neurons and electrophysiological characterization of recombinant VDAC channels.

Nevertheless, these approaches do not substitute for direct demonstration of STX–VDAC signaling in primary POMC neurons or in vivo. We have therefore revised the Discussion to emphasize that establishing the physiological significance of this mitochondrial pathway will require validation in primary neuronal preparations and whole-animal models.

> *(2) Structural Binding Site of STX on VDAC*
>
> *The exact structural binding site of STX on VDAC remains unresolved.*

We agree. BF-STX chemoproteomics identifies proteins interacting with STX in a cellular environment but does not resolve the amino acid residues or structural pocket responsible for binding.

We have clarified this limitation in the Discussion. Determining the STX-binding site will require complementary approaches such as targeted mutagenesis, direct binding measurements with purified VDAC proteins, and structural studies in membrane-like environments, including lipid nanodiscs. Such studies should also determine whether STX recognizes a conserved feature among VDAC isoforms or exhibits isoform selectivity.

> *(3) Lack of VDAC2 Loss-of-Function Experiments*
>
> *No loss-of-function experiments (e.g., VDAC2 knockdown) were performed to establish a direct causal link between VDAC2 and STX's bioenergetic and neuroprotective effects.*

We agree that VDAC loss-of-function experiments would provide an important additional test of causality.

Our present evidence is convergent: chemoproteomics identifies VDAC proteins as STX-interacting targets; single-cell analyses demonstrate VDAC expression in POMC neurons; electrophysiological studies show that STX modifies VDAC channel properties; and metabolic analyses demonstrate STX-dependent changes in mitochondrial bioenergetics. Together, these findings support a STX–VDAC mechanism but do not establish that VDAC2 alone is necessary for the mitochondrial or neuroprotective actions of STX.

We have revised the manuscript accordingly and explicitly identify the absence of loss-of-function experiments as a limitation.

Because whole-body VDAC2 loss-of-function is associated with severe developmental consequences, future studies will require conditional or neuron-specific approaches. Parallel evaluation of VDAC1 and VDAC3 will also be important because all three isoforms were identified by chemoproteomics and potential functional redundancy may complicate single-isoform manipulations.

> *(4) Non-linear Dose-Response at Higher STX Concentrations*
>
> *The non-linear dose-response at higher STX concentrations also requires further investigation.*

We agree that the non-linear concentration-response warrants further investigation and have revised the Discussion to avoid interpreting the STX response as a simple monotonic concentration-response relationship.

One possibility is that STX engages multiple mitochondrial targets with different apparent affinities and opposing effects on respiration. At lower concentrations, STX may preferentially engage a higher-affinity target, potentially VDAC, whereas higher concentrations may recruit lower-affinity targets that constrain this response. Consistent with this possibility, our BF-STX dataset (Supplemental Tables) identified several mitochondrial proteins involved in oxidative phosphorylation and metabolite transport, including ATP5F1C, NNT, SLC25A4, SLC25A5 and SLC25A3. ATP5F1C is required for efficient mitochondrial ATP production (Fiorillo, Scatena et al. 2021), and estrogenic regulation of ATP synthase has been reported (Massart, Paolini et al. 2002, Moreno, Moreira et al. 2013). NNT, SLC25A4, SLC25A5 and SLC25A3 also regulate mitochondrial respiration, redox balance, and ATP production (Mayr, Merkel et al. 2007, Lopert and Patel 2014). However, BF-STX enrichment does not establish direct STX binding, relative affinity, or functional modulation of these proteins. We therefore present the multi-target explanation only as a hypothesis. Direct binding and concentration-dependent target-engagement studies will be required to determine whether the non-linear response reflects recruitment of a lower-affinity mitochondrial target, concentration-dependent effects on VDAC itself, or downstream mitochondrial feedback.

We thank the editors and reviewers again for their constructive comments. The revised manuscript more clearly defines the physiological rationale for the experimental system, establishes the scope of the STX–VDAC mitochondrial mechanism supported by our data, and places its potential relevance to neurodegeneration in an appropriately forward-looking context.

References cited in the response

Do, K., B. T. Laing, T. Landry, W. Bunner, N. Mersaud, T. Matsubara, P. Li, Y. Yuan, Q. Lu and H. Huang (2018). "The effects of exercise on hypothalamic neurodegeneration of Alzheimer's disease mouse model." PLoS One 13(1): e0190205.

Fiorillo, M., C. Scatena, A. G. Naccarato, F. Sotgia and M. P. Lisanti (2021). "Bedaquiline, an FDA-approved drug, inhibits mitochondrial ATP production and metastasis in vivo, by targeting the gamma subunit (ATP5F1C) of the ATP synthase." Cell Death Differ 28(9): 2797-2817.

Kleiner, P., W. Heydenreuter, M. Stahl, V. S. Korotkov and S. A. Sieber (2017). "A Whole Proteome Inventory of Background Photocrosslinker Binding." Angew Chem Int Ed Engl 56(5): 1396-1401.

Lee, H.-J., Z. Bostick, J. Doherty, T. L. Swanson, M. J. Kelly, J. F. Quinn, N. E. Gray and P. F. Copenhaver (2025). "Neuroprotection against beta-amyloid toxicity by the novel estrogen

receptor modulator STX requires convergent signaling pathways." Frontiers in Molecular Neuroscience Volume 18 - 2025.

Lopert, P. and M. Patel (2014). "Nicotinamide nucleotide transhydrogenase (Nnt) links the substrate requirement in brain mitochondria for hydrogen peroxide removal to the thioredoxin/peroxiredoxin (Trx/Prx) system." J Biol Chem 289(22): 15611-15620.

Massart, F., S. Paolini, E. Piscitelli, M. L. Brandi and G. Solaini (2002). "Dose-dependent inhibition of mitochondrial ATP synthase by 17 beta-estradiol." Gynecol Endocrinol 16(5): 373-377.

Mayr, J. A., O. Merkel, S. D. Kohlwein, B. R. Gebhardt, H. Böhles, U. Fötschl, J. Koch, M. Jaksch, H. Lochmüller, R. Horváth, P. Freisinger and W. Sperl (2007). "Mitochondrial phosphate-carrier deficiency: a novel disorder of oxidative phosphorylation." Am J Hum Genet 80(3): 478-484.

Moreno, A. J., P. I. Moreira, J. B. Custódio and M. S. Santos (2013). "Mechanism of inhibition of mitochondrial ATP synthase by 17β-estradiol." J Bioenerg Biomembr 45(3): 261-270.

Shen, Y., M. Tian, Y. Zheng, F. Gong, A. K. Y. Fu and N. Y. Ip (2016). "Stimulation of the Hippocampal POMC/MC4R Circuit Alleviates Synaptic Plasticity Impairment in an Alzheimer's Disease Model." Cell Rep 17(7): 1819-1831.

https://doi.org/10.7554/eLife.111731.1.sa3